PNAS
www.pnas.org

SUPPLEMENTARY INFORMATION for

Calcium modulates the domain flexibility and function of an α-actinin similar to the ancestral α-actinin

Nikos Pinotsis, Karolina Zielinska, Mrigya Babuta, Joan L. Arolas, Julius Kostan, Muhammad Bashir Khan, Claudia Schreiner, Anita Salmazo, Luciano Ciccarelli, Martin Puchinger, Eirini A. Gkougkoulia, Euripedes de Almeida Ribeiro Jr, Thomas C. Marlovits, Alok Bhattacharya & Kristina Djinovic-Carugo

Correspondence to Kristina Djinovic-Carugo

Email: kristina.djinovic@univie.ac.at

This PDF file includes:

www.pnas.org/cgi/doi/10.1073/pnas.1917269117

SUPPLEMENTARY MATERIALS and METHODS

Protein production and purification

The coding sequence of WT *Eh*Actn2 containing F247L and E435G with respect to UP code C4LWU6 was kindly provided by Lars Backman (Umeå University, Sweden) and cloned into pET-19b (Novagen) and pETM-14 (EMBL) vectors. These constructs were used as templates to generate all other constructs used in this work (see Table S1). Proteins were typically expressed overnight at 20°C using LB or auto-induction media in *Escherichia coli* strain Rosetta2(DE3)pLysS, except EF-hands, which were expressed in strain BL21(DE3)pLysS. Se-Met variants of rod and *Eh*Actn2 were similarly produced in *E. coli* B834(DE3) cells grown in minimal medium (Molecular Dimensions) supplemented with Se-Met. Cells were re-suspended in buffer A (50 mM Tris-HCl, pH 7.5, 150 mM NaCl, 20 mM imidazole, 1 mM dithiothreitol (DTT)) plus protease inhibitors cocktail including 1 mM phenylmethanesulfonylfluoride (PMSF). In selected cases buffer A was supplemented with 5% (v/v) glycerol, 0.1% (v/v) Triton X-100 and 0.5 mM EDTA. Cells were disrupted and cell debris removed by centrifugation. Supernatant was subsequently loaded onto a 5-ml His-Trap FF crude column (GE Healthcare) previously equilibrated with buffer A and the sample eluted with the same buffer plus 400 mM imidazole. The N-terminal His-tag was next cleaved using TEV or 3C protease by overnight dialysis at 4°C against buffer A, which in selected cases was supplemented with 1 mM PMSF. The digested sample was loaded onto a Ni Sepharose 6 Fast Flow column (GE Healthcare) previously equilibrated with buffer A to remove uncleaved protein and His_6-tagged protease. An additional 1-ml GSTrap Fast Flow column (GE Healthcare) was connected in line with the Ni Sepharose column to remove the GST-tagged 3C protease. Flow-through was diluted with 20 mM Tris-HCl, pH 7.6 to 25 mM NaCl, loaded onto a 6-ml Resource Q column (GE Healthcare), and further eluted with a 0-100% gradient of the same buffer plus 1 M NaCl. Protein fractions were pooled and finally loaded onto a Superdex 200 26/600 column (GE Healthcare) previously equilibrated with buffer B (20 mM Tris-HCl, pH 7.6, 150 mM NaCl). For crystallographic studies, both *Eh*Actn2 and ΔCa were dialyzed against 50 mM HEPES, pH 7.5, methylated as published elsewhere (1), and further polished by SEC as described above.

Before each experiment all protein samples were dialyzed against specific buffers (see below) and concentrated by ultrafiltration. Protein identity and purity were analysed by SDS-PAGE. For calculation of molar protein concentration, individual proteins were considered in their respective oligomeric state (*i.e.* dimer for *Eh*Actn2). To verify the presence of disulphide bonds, samples at 1 mg/ml were incubated at room temperature (RT) for 1 h in the absence and presence of 0.5 mM oxidized glutathione and analysed by SDS-PAGE using loading buffer with and without β-mercaptoethanol. The presence of Ca^{2+} in *Eh*Actn2 and EF1-4 was assessed by intact mass spectrometry at the Mass Spectrometry Service Facility (MFPL, Vienna).

Static and dynamic light scattering

Static light scattering was performed at RT by SEC-MALS using a Superdex 200 10/300 Increase column (GE Healthcare) previously equilibrated with buffer B plus 5 mM EGTA or 5 mM $CaCl_2$. Samples were loaded at 4 mg/ml using an Agilent Technologies 1260 Infinity HPLC system coupled to a MiniDawn Treos detector (Wyatt) with a laser emitting at 690 nm. The refractive index was measured with an RI-101 detector (Shodex). Samples for dynamic laser light scattering were prepared at 0.5-5 mg/ml in buffer B and

measured at RT using a DynaPro Nanostar instrument (Wyatt Technology) with a laser wavelength of 658 nm. Data were analysed with DYNAMICS software (Wyatt Technology).

CD spectroscopy

Far-UV CD spectra were acquired at RT using a Chirascan Plus spectrophotometer (Applied Photophysics). Samples were prepared in buffer B and diluted to 10 μM in 1 mM EGTA or 1 mM $CaCl_2$. Spectra were collected and 200-260 nm using a 0.1 mm path-length quartz cuvette and 1 nm intervals.

Differential scanning fluorimetry

Proteins were first dialyzed against buffer B and then mixed (4 μl at 2 mg/ml) in the same buffer with 1 μl of 20x SYPRO Orange protein gel stain (ThermoFisher Scientific) to a final volume of 25 μl. Measurements were carried out in triplicate in 1 mM EGTA, 1 mM $CaCl_2$ or 0.2 mM EGTA plus 2 mM $MgCl_2$. Fluorescent signal was measured using iQTM5 multicolour Real-Time PCR Detection System (Bio-Rad) and data analysed using Bio-Rad CFX Manager software.

Limited proteolysis experiments

Proteins at 1 mg/ml were digested in 50 mM Tris, pH 8.0 in 5 mM $CaCl_2$ or 0.5 mM EGTA plus 5 mM $MgCl_2$ using bovine pancreatic trypsin, bovine pancreatic chymotrypsin, proteinase K from *Engyodontium album*, subtilisin from *Bacillus licheniformis*, and thermolysin from *B. thermoproteolyticus* (all from Sigma-Aldrich). Reactions were incubated at RT for 1 h using protease:substrate weight ratios of 1:50 and 1:100. Samples were subsequently precipitated with trichloroacetic acid and analysed by SDS-PAGE. Selected bands were identified by peptide mass fingerprinting at the Mass Spectrometry Service Facility.

Isothermal titration calorimetry

ITC was conducted using a MicroCal iTC200 calorimeter (Malvern Instruments) at both 25°C and 37°C in buffer C (20 mM HEPES, pH 8.0, 100 mM KCl). Before measurements samples were polished by SEC in 10 mM EGTA or 10 mM EDTA in order to completely remove Ca^{2+} from the protein. Absence of EGTA/EDTA bound to samples was confirmed by intact mass spectrometry. All buffers were passed through a Chelex 100 column (Bio-Rad) to remove metal traces. Ca^{2+} binding affinity was quantified using protein at 20, 100 and 500 μM titrating with 0.2, 1 and 5 mM $CaCl_2$, respectively. Mg^{2+} binding affinity was similarly quantified using protein at 100 μM titrating with 1 mM $MgCl_2$. For competition experiments, protein at 100 μM was titrated with 1 mM $CaCl_2$ plus 1 mM $MgCl_2$. To measure protein-protein affinity, protein at 35 μM was titrated with protein at 350 μM in 1 mM $CaCl_2$ or 1 mM EGTA. All measurements were performed at least in triplicate. To account for dilution heat, each ligand was titrated into buffer C and the signal was subtracted. Binding parameters were obtained using a single-site model using Origin software (Origin Lab).

Fluorescence assays

Amount of Ca^{2+} bound to protein was measured using the high Ca^{2+}-affinity dye Quin-2 (Sigma-Aldrich). Quin-2 was serially diluted in buffer D (20 mM Tris-HCl, pH 8.0, 100 mM KCl) previously treated with Chelex 100 resin (BioRad) to a concentration of 88 μM. Dye concentration was determined by measuring the absorbance at 240 nm using $\varepsilon=4.2 \times 10^4\ M^{-1}\ cm^{-1}$. Ca^{2+} standards and boiled protein samples were prepared in buffer D plus 4 M urea and subsequently diluted 1:10 with Quin-2. Fluorescence measurements were

performed at 20°C using a 10 mm path-length cuvette and a Perkin Elmer LS50B fluorimeter at λ_{ex}= 331 nm and λ_{em}=500 nm.

Ca^{2+}-dye competition assays were carried out using the low Ca^{2+}-affinity dye Oregon Green 488 BAPTA-5N (Thermo Fisher Scientific), which was initially dissolved in dimethylformamide and later diluted in buffer D previously treated with Chelex 100 resin to a concentration of 6.5 μM. Dye concentration was determined spectrophotometrically at 494 nm using ε=7.65 x 10^4 M^{-1} cm^{-1}. Affinity of dye for Ca^{2+} in buffer D was found to be 4 μM in good agreement with the manufacturer's specifications. In the assays, increasing protein concentrations were added to Chelex-treated buffer D containing 2.5 μM Ca^{2+}. Dye at final concentration of 260 nM was next added to protein-Ca^{2+} mixtures, and fluorescence was measured at 20°C using a 10 mm path-length cuvette and same fluorimeter as above at λ_{ex}= 494 nm and λ_{em}=520 nm. Normalised fluorescence intensity values were fitted using a one-site competition model in SigmaPlot software (Systat Software).

For time-resolved fluorescence anisotropy experiments, ^{4}*Eh*Actn2 and ^{4}NEECK at 10 μM were N-terminally labelled with Atto 488 dye using 20 μM sortase A and 100 μM LPETGG peptide conjugated to Atto 488 in 1x sortase buffer (50 mM Tris-HCl, pH 8.0, 150 mM NaCl, 10 mM $CaCl_2$). Unreacted labelling peptide and sortase were separated using a Superdex 200 10/300 column previously equilibrated in buffer B. Data was acquired using an Olympus iX71 inverted microscope equipped with an Ultra-Plan-Super Apochromat water immersion objective (UPLSAPO 60xW, NA 1.2) and coupled to a MicroTime200 TCSPC module (PicoQuant GmbH), which was controlled by the PicoQuant Symphotime software. All measurements were performed at 20°C in a 384-well sensoplate plus (Greiner Bio-one GmbH) in buffer B plus 1 mM $CaCl_2$ or 1 mM EGTA. Samples were excited with a 481 nm-pulsed diode laser in pulsed-interleaved excitation (PIE) regime, and the vertical and horizontal polarized intensities at 525/45 nm were monitored separately with two PicoQuant PMA Hybrid 40 detectors. Data was fitted with the FluoFit decay analysis software package from PicoQuant using the first order exponential decay function y(t) = A1 exp(-t/t) + y0.

Co-sedimentation assays for F-actin bundling

Rabbit skeletal muscle G-actin was either purified from acetone powder (kindly provided by Matthias Rief, Technische Universität München, Germany) as previously described (2) or purchased from Hypermol. Before assays, G-actin was dialyzed overnight at 4°C against G-Buffer (2 mM Tris-HCl, pH 8.0, 0.2 mM $CaCl_2$, 0.2 mM ATP, 2 mM β-mercaptoethanol) while α-actinin constructs were prepared in buffer D. All proteins were then centrifuged at 125,000x*g* for 1 h at 4°C. G-actin was polymerized into F-actin by addition of 1/10^{th} volume of 10x F-Buffer (50 mM Tris-HCl, pH 8.0, 0.5 M KCl, 20 mM $MgCl_2$, 20 mM ATP). As typically done in F-actin bundling co-sedimentation assays, a fixed concentration of F-actin (4 μM) was mixed with increasing concentrations of α-actinin constructs (0.01875-3 μM) in G-Buffer containing 1 mM EGTA or 1 mM $CaCl_2$. To assess the effect of Mg^{2+}, the assay was performed in 1 mM EGTA or 1 mM EGTA plus 2 mM $MgCl_2$. For "rescue" experiments, EF1-2 or EF1-4 in 20-fold molar excess were first incubated for 10 min with 1 mM $CaCl_2$ or 1 mM EGTA. ΔEF1-4 or ΔEF3-4 were subsequently added to the reactions and incubated for 1 h at RT. Next, F-actin was added to the mixture and incubated for an additional hour at RT before centrifugation at 18,000x*g* for 20 min at 20°C. Supernatant was then transferred to new tubes and diluted with 2x loading buffer. Equivalent amount of 1x loading buffer was added to pellet fractions. Actin in supernatant and pellet was quantified using a LabChip GX II Touch HT instrument (PerkinElmer). All

experiments were performed at least in triplicate. For comparison, selected samples were analysed by SDS-PAGE and protein bands quantified by scanning.

Electron microscopy

For EM of negatively stained proteins, 0.25 μM of α-actinin construct was mixed with 4 μM F-actin (prepared as above) and incubated for 1 h at RT. Samples were prepared by applying 3 μl of protein solution on previously glow discharged carbon-coated copper grids and negatively stained with 2% uranyl acetate. Dilutions were optimized to ensure a good distribution of the sample across the grid. Grids were imaged under low dose conditions with a Tecnai Morgagni 80 KV electron microscope at a defocus range of 2.0-5.0 μm and at a nominal magnification of 15,200x resulting in a pixel size of 5.89Å on the specimen.

Co-sedimentation assays for F-actin binding

Before assays, G-actin was polymerized by addition of $1/10^{th}$ volume of 10x F-buffer and subsequently depolymerized by extensive dialysis against G-buffer to ensure the presence of polymerizable actin only. A fixed concentration of α-actinin construct (3 μM) in buffer D was mixed with increasing concentrations of G-actin (0-30 μM) in G-Buffer containing 1 mM EGTA or 1 mM $CaCl_2$ to avoid precipitation problems with α-actinin constructs at high protein concentration. G-actin was polymerized into F-actin by addition of $1/10^{th}$ volume of 10x F-Buffer. Samples were incubated for 1 h at RT and centrifuged at 125,000x*g* for 30 min at 22°C. Supernatant was then transferred to new tubes and diluted with 2x loading buffer. Supernatant and pellet fractions were analysed as in F-actin bundling experiments (see above). Quantification was performed assuming a 1:1 actin:α-actinin stoichiometry. Binding curves were generated using SigmaPlot software assuming a one-site saturation model.

Rheology

Rheological measurements were carried out on an Anton Paar Modular Compact Rheometer MCR 102 equipped with a CP25-1 spindle (25 mm plate diameter, 1 degree angle) and analysed using RheoPlus software. Before assays, G-actin (Hypermol) and various α-actinin constructs were dialysed overnight at 4°C against 2 mM Tris-HCl, pH 8.0, 0.2 mM $CaCl_2$, 0.2 mM ATP, 5 mM β-mercaptoethanol. All proteins were then centrifuged at 125,000x*g* for 1 h at 4°C. G-actin (at final concertation of 15 μM) was mixed with α-actinin constructs (0-30 μM) and polymerization initiated by addition of $1/10^{th}$ volume of 20 mM Tris-HCl, pH 8.0, 1 M NaCl, 10 mM $MgCl_2$, 10 mM $CaCl_2$. The sample (90 μl) was immediately applied to the plate of the rheometer and incubated overnight without shearing at 25°C in the instrument before starting the first measurement. To minimize dehydration, sample was sealed with paraffin oil. Frequency sweeps (0.001-10 rad/s) were done in controlled strain mode with maximum shear strain of 1%. The magnitude of the complex modulus was reproducible to within a factor of 2 and the phase shift within 10% in three repetitions of the rheological experiments.

Small-angle X-ray scattering

SAXS data was collected at 20°C on a Pilatus 1M detector at ESRF (France) beamline BM29. Samples were prepared at 0.6, 2.4 and 3.6 mg/ml in buffer B plus 5 mM EGTA or 5 mM $CaCl_2$. Molecular parameters were calculated with PRIMUS and GNOM, while atomic structures were fitted to experimental SAXS data using CRYSOL (all from ATSAS program suite (3)).

Protein crystallization and X-ray data collection

Crystallization screens were performed by the sitting-drop vapor-diffusion method by mixing equal volumes of protein solution (15 mg/ml for ABD and rod; 5 mg/ml for *Eh*Actn2 and ΔCa) and precipitant. Crystals of ABD appeared at 4°C in 0.1 M sodium cacodylate (pH 6.5), 0.2 M calcium acetate, 40% (v/v) PEG 600 as reservoir solution. Crystals of rod were obtained at 22°C in 0.1 M HEPES (pH 6.5), 0.2 M $MgCl_2$, 25% (w/v) PEG 3,350, which were cryo-protected with 10% (v/v) MPD. Crystals of Se-Met rod variant were obtained at 22°C in 0.1 M HEPES (pH 7.5), 50 mM $MgCl_2$, 30% (v/v) PEG MME 550. Crystals of *Eh*Actn2 appeared at 4°C in 92 mM bicine/trizma base (pH 8.5), 27.6 mM $CaCl_2$, 27.6 mM $MgCl_2$, 11.5% (w/v) PEG 3,350, 11.5% (w/v) PEG 1,000, 11.5% (v/v) MPD. Crystals harvested after 4-7 days usually belonged to the tetragonal lattice, while those harvested at a later stage belonged to the orthorhombic lattice. Crystals of Se-Met *Eh*Actn2 variant grew at 22°C in similar conditions containing 64 mM of bicine/trizma base (pH 8.5), 18.4 mM $CaCl_2$, 18.4 mM MgCl2, 8% (w/v) PEG 3,350, 8% (w/v) PEG 1,000, 8% (v/v) MPD. Crystals of ΔCa were obtained at 20°C in 0.1 M bis-tris (pH 5.5), 0.3 M $MgCl_2$, 20% (w/v) PEG 3,350. Crystals of both *Eh*Actn2 and ΔCa were cryo-protected with 20% (v/v) glycerol. Selected harvested crystals were analysed by Silver-stained SDS-PAGE in order to confirm protein integrity. Crystals were diffracted using different wavelengths and detectors at ESRF, Diamond (UK) and SLS (Switzerland) (see Table S2).

Structure determination and refinement

Diffraction data were processed with the XDS package (4) (see Table S2 for data processing statistics). The structure of ABD was determined by molecular replacement using program MOLREP (5) and the ABD from α-actinin-3 (PDB 1WQU) as search model. Two copies of ABD were positioned in the asymmetric unit and the structure was further improved by refinement using PHENIX (6) and manual building using COOT (7). The model for ABD covers residues 2-231. The structure of the rod domain was solved by SAD. Ten out of the theoretical 12 selenium positions were determined using program SHELXD (8) with a $CC_{all/weak}$=41.8/20.6. Phasing and density modification were performed using the AutoSol script from PHENIX by combining the SAD dataset with the high-resolution dataset. The final figure of merit for phasing was 0.77, rendering a clear density map for main chain and side chain atoms. A preliminary model encompassing 80% of the structure was build using program ARP/wARP (9), which was then used as starting model for refinement using PHENIX and manual building using COOT. The model for rod covers residues 243-477 for chain A and residues 248-476 for chain B.

The structure of *Eh*Actn2 in the tetragonal lattice was also solved by SAD. Eight out of the theoretical 16 selenium positions were identified by SHELXD with a $CC_{all/weak}$=52.7/23.5. Phasing and density modification were performed using AutoSol PHENIX including the positions of the selenium atoms found by SHELXD. This resulted in a final figure of merit for phasing of 0.77 and a very clear density map of the main chain atoms. The refined models from ABD and rod were placed in the electron density using MOLREP and the model was further refined against the native data including the phases from the SAD dataset. Missing parts of the structure were built manually using COOT. The structure was finalised by refinement using PHENIX with restraints from ABD and rod models and manual building using COOT. To assess the identity of Ca^{2+}, we calculated anomalous difference Fourier maps for the dataset collected at long wavelength combined with phases from the finalised *Eh*Actn2 model lacking any bound ligands and atoms using programs SFALL and FFT from CCP4 (10). The model for *Eh*Actn2 covers residues 1-618.

The structures of orthorhombic *Eh*Actn2 and ΔCa were determined by molecular replacement using program PHASER (11) and the rod as search model. Large parts of the CaMD lobes were placed in the electron density using real space refinement in COOT. Electron density was not of sufficient quality for placing the ABD and therefore the partial models were refined using the LORESTR Pipeline in Refmac5 (12). The generated maps were of sufficient quality to place the ABD using phased molecular replacement with MOLREP. The structures were finalised by refinement in the LORESTR Pipeline and manual building using COOT. Orthorhombic *Eh*Actn2 and ΔCa models cover residues 1-618 and 1-617, respectively. Table S2 provides data on final model refinement statistics for all structures.

Structure analysis and bioinformatics

Protein-protein interfaces were analysed using the PISA server (13). Structural alignments and assignment of secondary structure elements were performed with PDBeFOLD (14). Protein domains and bending hinges were calculated with DynDom (15). Figures were generated with PyMOL (http://www.pymol.org/). Calculation of protein electrostatic surface was performed with APBS and PDB2PQR (16, 17). Calculation of EF-hands angles θ, ϕ, ω was performed with program VGM as reported elsewhere (18). For structure comparison we used m-score, defined as the fraction of the maximal number of residues that are superposable, and can be computed as

$$m\text{-}score = \frac{n_a}{min(n_1,n_2)}$$

where n_a residues of two proteins of n_1 and n_2 residues are aligned (19).

Growth and transfection of *E. histolytica*

E. histolytica strain HM-1:IMSS trophozoites and all transformed strains were grown and maintained in TY1-S-33 medium as previously described (20). Constructs containing a C-terminal HA tag were cloned at BamH1/Kpn1 sites into EhNeo-GFP vector (21), which contains a constitutive promoter and G418 as selection agent, and was kindly provided by Nancy Guillen (Pasteur Institute, France). *E. histolytica* trophozoites were transfected by electroporation as previously described (20). Transfected cells were grown for 24 h (until 60-70% confluency) in 10 µg/ml G418 followed by induction with 30 µg/ml G418 for 48 h.

Antibody purification and immunofluorescence staining

*Eh*Actn2 antibody was raised in mice using recombinant rod domain and next affinity purified from crude serum by immunoblotting. Briefly, 500 µg of rod domain were run on SDS-PAGE and transferred onto a polyvinylidinefluoride (PVDF) membrane. Protein band was identified using Ponceau staining, cut and washed twice with 1x TBS-Tween 20 buffer. After blocking for 2 h at RT with 1x TBS-Tween 20 plus 5% BSA, the strip was incubated with 1 ml of crude serum overnight at 4°C using a rotating shaker. The strip was subsequently washed twice with 1x PBS and twice with 1x TBS-Tween 20, each for 5 min. Antibody was finally eluted with glycine buffer (pH 2.0) and the reaction immediately neutralised with 1 M Tris-HCl (pH 8.0). Immunofluorescence staining of *E. histolytica* trophozoites was carried out as previously described (20). Confocal images were visualised using an Olympus Fluoview FV1000 laser scanning microscope. Used antibody dilutions were as follows: affinity-purified anti-*Eh*Actn2 at 1:25; anti-EhTMKB1-9 at 1:50; anti-

EhCaBP1 at 1:100; anti-HA (from Sigma-Aldrich) at 1:200; anti-rabbit/mice Alexa Fluor 488 and anti-mice Alexa Fluor 405 (Jackson ImmunoResearch Laboratories) at 1:200; anti-TRITC-Phalloidin at 1:250.

Western blotting and erythrophagocytosis assays

Total cell lysates for Western blotting were prepared as previously described (22). For immunoblotting, 50 µg of cell lysate were run on SDS-PAGE, which was then transferred onto a PVDF membrane. Antigens were detected using anti-HA and anti-*Eh*Coactosin antibodies at 1:500 and 1:10000, respectively, followed by addition of secondary anti-mice HRPO-conjugated antibody (Sigma-Aldrich) at 1:10,000, and visualised with ECL reagents (Millipore). Erythrophagocytosis assay using *E. histolytica* trophozoites and RBCs were carried out as previously reported (20).

Statistical analysis

Shaprio-wilk test was performed to determine the distribution of the data. Statistical comparisons for a skewed distribution were performed using Kruskal-Wallis test followed by Dunn's multiple comparison test. One-way Anova was performed for normally distributed data as indicated. Differences in mean values were considered significant at *p-value$\leq$0.05, **p-value$\leq$ 0.005 and ***p-value$\leq$ 0.0005. All calculations of statistical significance were performed using GraphPad software 8 (Prism). PCC was obtained using Olympus Fluoview FV1000 software and plots were generated with Image J software (http://rsb.info.nih.gov/ij/).

SUPPLEMENTARY TABLES

Table S1. Constructs used in this work

Name	Sequence	MW (kDa)	Mutations	Vector	Protein tag(s)
*Eh*Actn2	1-619	140		pET-19b	N-t His_{10}+TEV
ΔCa	1-619	140	D497N+N499G+D501N	pET-19b	N-t His_{10}+TEV
NEECK	1-619	140	A241E+L245E	pET-19b	N-t His_{10}+TEV
NEECK[#]	1-619	140	A241E	pET-19b	N-t His_{10}+TEV
[4]*Eh*Actn2	4-619	139		pET-19b	N-t His_{10}+TEV
[4]NEECK	4-619	139	A241E+L245E	pET-19b	N-t His_{10}+TEV
ΔEF3-4	1-561	127		pET-19b	N-t His_{10}+TEV
ΔEF1-4	1-480	108		pET-19b	N-t His_{10}+TEV
ΔEF3-4 SS1	1-561	127	S322C+Q473C	pET-19b	N-t His_{10}+TEV
ΔEF3-4 SS2	1-561	127	G326C+Q473C	pET-19b	N-t His_{10}+TEV
ΔEF3-4 SS3	1-561	127	Q319C+Y469C	pET-19b	N-t His_{10}+TEV
*Eh*Actn2-HA	1-619	142		pET-19b	N-t His_{10}+TEV & C-t HA
ABD	3-231	26		pETM-14	N-t His_6+3C
ABD-SR1	1-367	42		pET-19b	N-t His_{10}+TEV
ABD-SR1 NEECK	1-367	42	A241E+L245E	pET-19b	N-t His_{10}+TEV
rod	240-480	55		pETM-14	N-t His_6+3C
rod SS1	240-480	55	S322C+Q473C	pETM-14	N-t His_6+3C
rod SS2	240-480	55	G326C+Q473C	pETM-14	N-t His_6+3C
rod SS3	240-480	55	Q319C+Y469C	pETM-14	N-t His_6+3C
EF1-2	480-561	9		pET-19b	N-t His_{10}+TEV
EF3-4	565-619	7		pET-19b	N-t His_{10}+TEV
EF1-4	480-619	16		pET-19b	N-t His_{10}+TEV
EF1-4 ΔCa	480-619	16	D497N+N499G+D501N	pET-19b	N-t His_{10}+TEV
EF1-4 D501N	480-619	16	D501N	pET-19b	N-t His_{10}+TEV
EF1-4 D505N	480-619	16	D505N	pET-19b	N-t His_{10}+TEV
chimActn2	1-245 (*Eh*Actn2) +272-742 (*h*Actn2) +457-619 (*Eh*Actn2)	202		pET-19b	N-t His_{10}+TEV
*Eh*Actn2-HA	1-619	142		EhNeo-GFP	C-t HA
ΔCa-HA	1-619	142	D497N+N499G+D501N	EhNeo-GFP	C-t HA
NEECK-HA	1-619	142	A241E+L245E	EhNeo-GFP	C-t HA
ΔEF3-4-HA	1-561	129		EhNeo-GFP	C-t HA

Table S2. Data collection and refinement statistics

	ABD (Native)	rod (SeMet)	rod (Native)	*Eh*Actn2 tetra (Native)	*Eh*Actn2 tetra (SeMet), peak	*Eh*Actn2 tetra (SeMet), low energy	*Eh*Actn2 ortho (Native)	ΔCa ortho (Native)
Data Collection								
Beamline	ID23-2 (ESRF)	ID14-1 (ESRF)	ID23-1 (ESRF)	I03 (Diamond)	ID14-4 (ESRF)	X06SA (SLS)	ID29 (ESRF)	ID30A-3 and ID23-1 (ESRF)
Detector	MX225 Rayonix	Q315r ADSC	Q315r ADSC	Pilatus 6M	Q315r ADSC	Pilatus 6M	Pilatus 6M	Pilatus 6M
Wavelength (Å)	0.87260	0.93340	0.97918	0.97860	0.978990	1.77125	1.00576	0.968620
Resolution Range (Å)	48.0-2.48 (2.54-2.48)[1]	46.81-2.05 (2.16-2.05)	48.30-2.87 (3.03-2.87)	41.65-3.10 (3.31-3.10)	49.03-4.27 (4.39-4.27)	48.86-4.29 (4.41-4.29)	46.24-3.10 (3.17-3.10)	46.85-3.30 (3.38-3.30)
Space group	*P 3*	*P 2_1 2_1 2_1*	*P 2_1 2_1 2_1*	*P 4_2 2_1 2*	*P 4_2 2_1 2*	*P 4_2 2_1 2*	*P 2 2 2_1*	*P 2 2 2_1*
Cell parameters a, b, c (Å)	146.74, 146.74, 33.97	46.08, 59.98, 187.25	46.15, 59.81, 193.21	192.3, 192.3, 57.17	191.88, 191.88, 57.05	190.77, 190.77, 56.89	43.21, 71.84, 241.70	40.74, 75.53, 234.25
Total reflections	85,073	158,985	140,950	174,399	103,243	200,858	100,558	69,098
Unique reflections	27,759	62,639	23,580	20,112	13,976	13,653	14,460	11,494
Multiplicity	3.1 (2.1)	2.5 (2.5)	6.0 (4.9)	8.7 (7.6)	7.4 (6.5)	14.7 (13.2)	7.0 (6.8)	6.0 (5.8)
Completeness (%)	95.6 (90.5)	99.6 (96.9)	99.2 (92.6)	100.0 (99.9)	99.1 (90.2)	99.5 (94.7)	99.1 (95.3)	99.1 (96.2)
Mean I/Sigma(I)	8.33 (2.0)	11.24 (1.8)	14.2 (3.3)	13.6 (1.3)	13.94 (4.17)	14.04 (3.36)	8.57 (0.48)	10.3 (1.40)
Wilson B-factor (Å^2)	51.4	31.31	75.80	114.0	135.4	136.1	126.6	120.1
R_{merge} (%)	10.1 (64.7)	6.0 (50.7)	8.0 (47.2)	10.9 (143.6)	9.3 (37.5)	14.3 (76.8)	13.3 (555.4)	8.4 (85.0)
$CC_{1/2}$ (%)	99.5 (39.8)	99.8 (68.3)	99.8 (85.3)	98.4 (71.4)	99.9 (98.7)	99.9 (96.6)	99.9 (43.3)	99.8 (76.9)
Software	XDS/XSCALE	XDS/Scala	XDS/Scala	XDS/Aimless	XDS/XSCALE	XDS/XSCALE	XDS/XSCALE	XDS/Aimless
Refinement								
R_{work} / R_{free} (%)	19.6 / 25.2	18.3 / 24.7		21.5 / 25.14			25.9 / 32.5	23.35 / 30.81
CC_{work} / CC_{free} (%)	96.1 / 93.3	96.3 / 93.2		96.3 / 95.7			95.1 / 87.7	94.5 / 92.2
Protein atoms	3,648	3,716		4,852			4,730	4,792
Solvent molecules	90	472						
Other atoms	1×Tris, 1×Ca^{2+}	2×βME		1×Ca^{2+}			1×Ca^{2+}	
B-factor (Å^2)								
Protein	61.95	37.50		117.2			82.7	212.3
Solvent	50.82	39.86						
Ramachandran Plot								
Favored (%)	96.93	99.78		97.06			94.81	95.60
Allowed (%)	3.07	0.22		2.76			4.38	3.75
Outliers (%)	0.00	0.00		0.17			0.81	0.65
Clashscore	8.10	4.74		7.82			20.51	22.47
Rmsd								
Bonds (Å)	0.008	0.008		0.003			0.013	0.006
Angles (°)	0.956	0.702		0.573			1.745	1.635
Software	PHENIX	PHENIX		PHENIX			Refmac5	Refmac5
PDB code	5NL7	5NL6		6SL2			6SL3	6SL7

[1]Values in parentheses refer to the highest-resolution shell.

Table S3. Structural similarity of ABDs

Protein[1]	Organism	RMSD (Å)	m-score	PDB code	Reference
Plectin-1	Human	1.099	0.9478	3F7P	(23)
Plectin-1	Mouse	1.144	0.9478	1SH5	(24)
α-Actinin-2	Human	1.188	0.9261	5A36	(25)
α-Actinin-1	Human	1.201	0.9261	2EYI	(26)
α-Actinin-3	Human	1.220	0.9422	1WKU	(27)
α-Actinin-4	Human	1.212	0.9295	2R0O	(28)
α-Actinin	Yeast	1.343	0.9214	5BVR	(29)
Filamin A	Human	1.533	0.9667	3HOR	(30)
Filamin B	Human	1.360	0.8826	3FER	-

[1]Chain with lowest RMSD value is considered for each protein.

Table S4. Analysis of protein domain interactions in the tetragonal *Eh*Actn2 structure

Interface Area [Å²][1]	3,684.5 (10.3%)			
ΔG [kcal/mol][2]	-12.3 (2.4%)			
ΔG P-value[3]	0.256			
CSS[4]	0.943			
Hydrogen bonds[5]				
	Protomer A	**Distance [Å]**	**Protomer B**	**Domain**
1	GLU 252 [OE2]	2.69	TYR 598 [OH]	neck-EF3-4
2	ARG 299 [NH1]	2.28	SER 448 [OG]	SR1-SR2
3	ARG 299 [NH1]	3.77	GLU 431 [OE1]	SR1-SR2
4	THR 315 [OG1]	2.91	GLN 491 [NE2]	SR1-EF1-2
5	ARG 325 [NE]	2.99	GLU 488 [OE2]	SR1-EF1-2
6	GLY 326 [O]	3.88	ASN 561 [ND2]	SR1-EF3-4
7	ARG 329 [NH2]	2.32	TRP 615 [O]	SR1-EF3-4
8	ARG 355 [NE]	3.89	ASP 451 [OD2]	SR1-SR2
9	ARG 355 [NH2]	3.77	ASP 451 [OD2]	SR1-SR2
10	ARG 358 [NE]	3.26	ASP 446 [O]	SR1-SR2
11	ARG 358 [NH2]	2.22	ASP 451 [OD2]	SR1-SR2
12	ASN 362 [ND2]	3.57	ASN 442 [O]	SR1-SR2
13	ASN 362 [ND2]	3.56	ASP 446 [OD1]	SR1-SR2
14	ARG 366 [N]	2.89	ASP 441 [OD2]	SR1-SR2
Salt bridges[5]				
1	LYS 289 [NZ]	3.99	GLU 440 [OE2]	SR1-SR2
2	ARG 299 [NE]	3.55	ASP 450 [OD2]	SR1-SR2
3	ARG 299 [NH1]	3.77	GLU 431 [OE1]	SR1-SR2
4	ARG 299 [NH1]	3.46	ASP 450 [OD2]	SR1-SR2
5	ARG 325 [NE]	2.99	GLU 488 [OE2]	SR1-EF1-2
6	ARG 325 [NE]	3.37	GLU 488 [OE1]	SR1-EF1-2
7	ARG 325 [NH1]	3.42	GLU 488 [OE2]	SR1-EF1-2
8	ARG 355 [NE]	3.89	ASP 451 [OD2]	SR1-SR2
9	ARG 355 [NH2]	3.77	ASP 451 [OD2]	SR1-SR2
10	ARG 358 [NH2]	3.33	ASP 451 [OD1]	SR1-SR2
11	ARG 358 [NH2]	2.22	ASP 451 [OD2]	SR1-SR2

[1]Percentage of total surface area involved in dimerization is shown in parenthesis.
[2]Percentage of solvation energy change due to interface formation is shown in parenthesis.
[3]P-value of the interface. P<0.5 denotes an interface with higher specificity than average hydrophobicity.
[4]Complex Formation Score.
[5]Hydrogen bonds and salt bridges are given for half of the structure (ABD-neck-SR1 plus SR2-CaMD). Total number of interactions is double based on internal two-fold symmetry of the structure.

Table S5. Inter-helical angles in the CaMDs of the three *Eh*Actn2 structures

	***Eh*Actn2 tetra**			***Eh*Actn2 ortho**			**ΔCa ortho**		
	θ (°)	**φ (°)**	**ω (°) (twist)**	**θ (°)**	**φ (°)**	**ω (°) (twist)**	**θ (°)**	**φ (°)**	**ω (°) (twist)**
EF1-2									
h1-h2	60.8	96.2	342	55.0	98.9	350	54.5	103.5	336
h2-h3	68.7	118.2	233	74.8	108.7	241	68.7	111.3	230
h1-h3	54.2	-118.6	114	54.9	-122.4	121	59.7	-111.6	106
h3-h4	66.1	92.4	357	69.7	83.5	357	65.0	91.6	352
h1-h4	59.9	103.0	239	55.8	96.4	244	56.2	101.8	235
h2-h4	156.0	-78.3	-82.2	151.7	-94.2	172	152.5	-89.2	165
EF3-4									
h1-h2	83.0	101.3	83	87.2	98.8	90	82.3	96.5	87
h2-h3	29.5	82.7	272	30.5	76.8	275	30.6	84.3	274
h1-h3	69.3	-105.1	220	65.0	-108.2	214	67.8	-110.1	224
h3-h4	96.5	68.2	22	97.9	70.7	16	96.5	66.4	14
h1-h4	14.3	139.9	276	17.5	148.4	273	13.8	136.9	275
h2-h4	110.7	-10.2	346	110.2	-17.3	342	11.2	-12.9	340
h4-h1[1]	146.9	148.3	326	143.2	170.9	322	150.9	170.8	323

[1]EF1-2 h4 with EF3-4 h1.

Table S6. ITC and thermodynamic data for protein-ion and protein-domain interactions

Titrant	Ligand	N	K_d (μM)	ΔH (cal/mol)	ΔS (cal/mol/deg)
EF1-4	Ca^{2+}	0.93 ± 0.02	0.0053[1] ± 0.003	-14,559 ± 2,576	N/D
EF1-4	Mg^{2+}	0.74 ± 0.09	9.39 ± 0.87	-4,217 ± 197	8.86 ± 0.84
EF1-4	Ca^{2+} + Mg^{2+}	0.65 ± 0.04	0.49 ± 0.13	-6,246 ± 165	7.95 ± 1.09
EF1-4 D501N	Ca^{2+}	0.93 ± 0.14	0.20 ± 0.04	-6,093 ± 232	10.20 ± 1.05
EF1-4 D505N	Ca^{2+}	0.89 ± 0.08	0.28 ± 0.20	-4,031 ± 224	16.73 ± 1.92
EF1-4 ΔCa	Ca^{2+}	N/D[2]	N/D	N/D	N/D
ABD-SR1 + Ca^{2+}	EF1-4	0.90 ± 0.05	3.68 ± 1.65	-77,700 ± 9,722	51.40 ± 5.85
ABD-SR1 + Ca^{2+}	EF3-4	N/D	48.50 ± 12.07	N/D	-145.2 ± 114.26
ABD-SR1-NEECK + Ca^{2+}	EF1-4	N/D	N/D	N/D	N/D
ABD-SR1 + EGTA	EF1-4	0.99 ± 0.11	8.3 ± 1.72	-28,400 ± 2,364	-71.00 ± 7.49
ABD-SR1 + EGTA	EF3-4	N/D	22.88 ± 2.90	N/D	-46.13 ± 18.01
ABD-SR1-NEECK + EGTA	EF1-4	N/D	N/D	N/D	N/D

[1] K_d for Ca^{2+} binding to EF1-4 calculated using a Mg^{2+}competition assay with AFFINIMeter software (Malvern Instruments). [2] N/D stands for not determined.

Table S7. Summary of interactions of EF-hands with the SR1-SR2/neck in the three *Eh*Actn2 structures

	Interface (A^2)	ΔG[1] (kcal/mol)	ΔG (kcal/mol) SR1-SR2/neck	ΔG (kcal/mol) EF1-4	ΔG (P-value)	NHB	NSB	CSS
***Eh*Actn2 tetra**	1,644.2	-19.4	8.99	10.4	0.188	8	4	0.951
***Eh*Actn2 ortho**	1,750.8	-21.9	9.37	12.58	0.320	10	5	1.000
ΔCa ortho	1,526.6	-13.4	6.69	6.67	0.455	10	3	1.000

[1]ΔG value does not include H-bonds (-0.44 kcal/mol per bond) and salt bridges (-0.15 kcal/mol per bridge). Total ΔG is the sum of all solvation energies from each residue that are involved in the interface. These are positive and make a negative contribution to the solvation energy gain of the interface. Higher contribution from each residue results in a stronger hydrophobic effect.

Table S8. Electrostatic interactions of EF-hands with the SR1-SR2/neck in the three *Eh*Actn2 structures

EF1-4	SR1-SR2	Distance (Å)			Interacting domains
		*Eh*Actn2 tetra	*Eh*Actn2 ortho	ΔCa ortho	
Hydrogen bonds					
VAL 481 [N]	SER 479 [O]	2.39	2.70	2.62	EF1-2/SR2
THR 482 [OG1]	GLU 476 [OE2]	3.78	-	2.91	EF1-2/SR2
ALA 483 [N]	GLU 476 [OE2]	3.25	2.45	3.31	EF1-2/SR2
GLU 484 [OE1]	ARG 325 [NH2]	-	3.54	-	EF1-2/SR1
GLU 484 [OE1]	TYR 469 [OH]	-	-	3.27	EF1-2/SR2
GLU 488 [OE2]	ARG 325 [NE]	2.99	3.37	-	EF1-2/SR1
GLN 491 [NE2]	THR 315 [OG1]	2.91	3.42	2.78	EF1-2/SR1
GLU 594 [OE2]	ARG 249 [NH1]	-	-	2.89	EF3-4/neck
SER 515 [OG]	GLN 319 [NE2]		2.94	2.98	EF3-4/SR1
MET 516 [O]	LYS 323 [NZ]	-	-	3.06	EF3-4/SR1
ASN 561 [ND2]	GLY 326 [O]	3.88	2.39	2.90	EF3-4/SR1
GLN 595 [NE2]	ASP 246 [OD1]	-	2.85	-	EF3-4/neck
TYR 598 [OH]	GLU 252 [OE2]	2.69	-	-	EF3-4/SR1
TRP 615 [O]	ARG 329 [NH1]	-	3.13	3.32	EF3-4/SR1
TRP 615 [O]	ARG 329 [NH2]	2.32	3.19	-	EF3-4/SR1
Salt Bridges					
VAL 481 [N]	GLY 480 [O]	2.25	2.26	2.26	EF1-2/SR2
GLU 594 [OE2]	ARG 249 [NH1]	-	-	2.89	EF1-2/neck
GLU 594 [OE2]	ARG 249 [NH2]	-	-	3.84	EF1-2/neck
GLU 484 [OE1]	ARG 325 [NH2]	-	3.54	-	EF1-2/SR1
GLU 488 [OE2]	ARG 325 [NE]	2.99	3.37	-	EF1-2/SR1
GLU 488 [OE1]	ARG 325 [NE]	3.37	-	-	EF1-2/SR1
GLU 488 [OE2]	ARG 325 [NH1]	3.42	-	-	EF1-2/SR1
HIS 500 [NE2]	GLU 464 [OE1]	3.45	-	-	EF1-2/SR2
HIS 500 [NE2]	GLU 464 [OE2]	3.98	-	-	EF1-2/SR2

SUPPLEMENTARY FIGURES

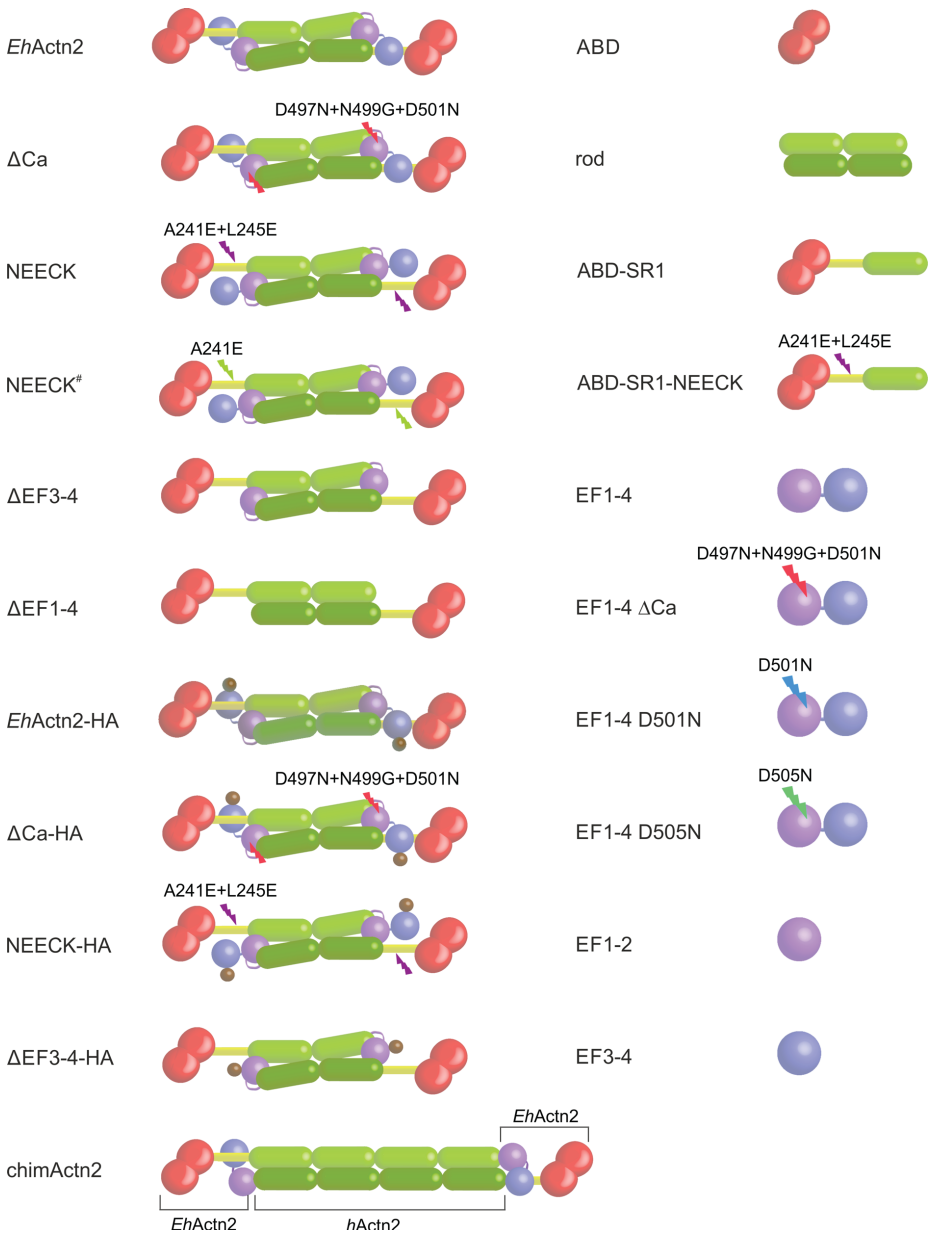

Figure S1. Constructs used in this work.
Schematics depicting the domain composition of *Eh*Actn2 constructs. ABD is shown in red, neck in yellow, rod (SR1-SR2) in green, EF1-2 in violet and EF3-4 in blue. Positions of mutated residues are indicated in each construct. The HA tag is shown as a brown sphere.

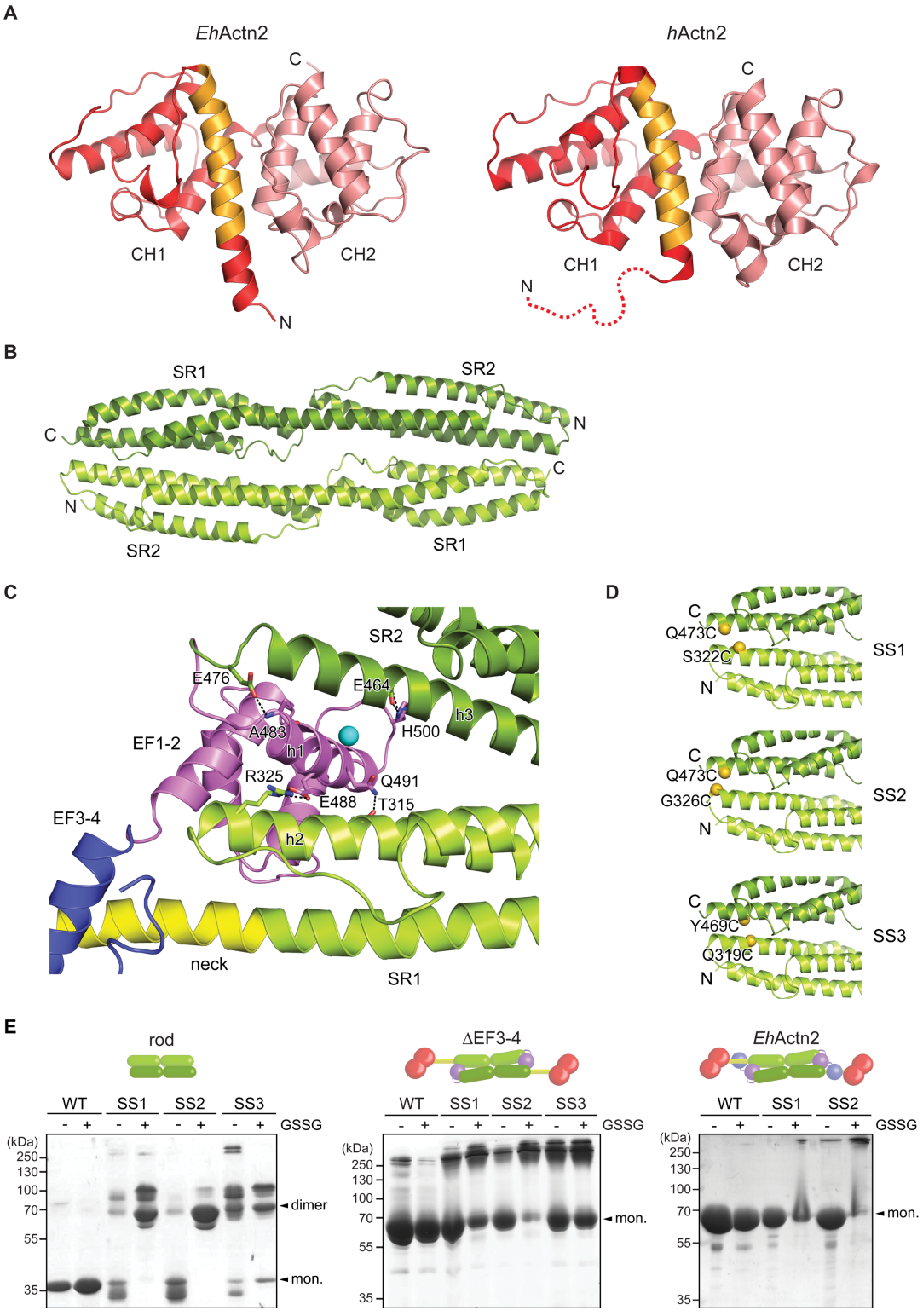

Figure S2. Structural features of individual EhActn2 domains.

(A) Comparison of ABD structures from *Eh*Actn2 and *h*Actn2 (PDB code 5A36) in a ribbon representation. ABS1 is coloured in orange as reference; the disordered N-terminal part of *h*Actn2 is shown as a dotted line. **(B)** When crystallized alone, the rod domain of *Eh*Actn2 forms an antiparallel dimer with an

interacting interface different to that in the full-length protein. **(C)** EF1-2 forms an extensive network of polar interactions with the SR from the adjacent protomer, which contributes to *Eh*Actn2 dimer stability. **(D)** Design of rod mutants with introduced pairs of cysteine residues based on the structure shown in (B). **(E)** Oligomerisation properties of cysteine mutants (for details on constructs, see Table S1) for the rod, ΔEF3-4 and *Eh*Actn2 as analysed by SDS-PAGE. Samples were incubated in the absence and presence of 0.5 mM oxidized glutathione (GSSG) to promote disulphide-bond formation. The presence of EF3-4 inhibits the formation of dimers. Monomeric and dimeric species are indicated for each sample.

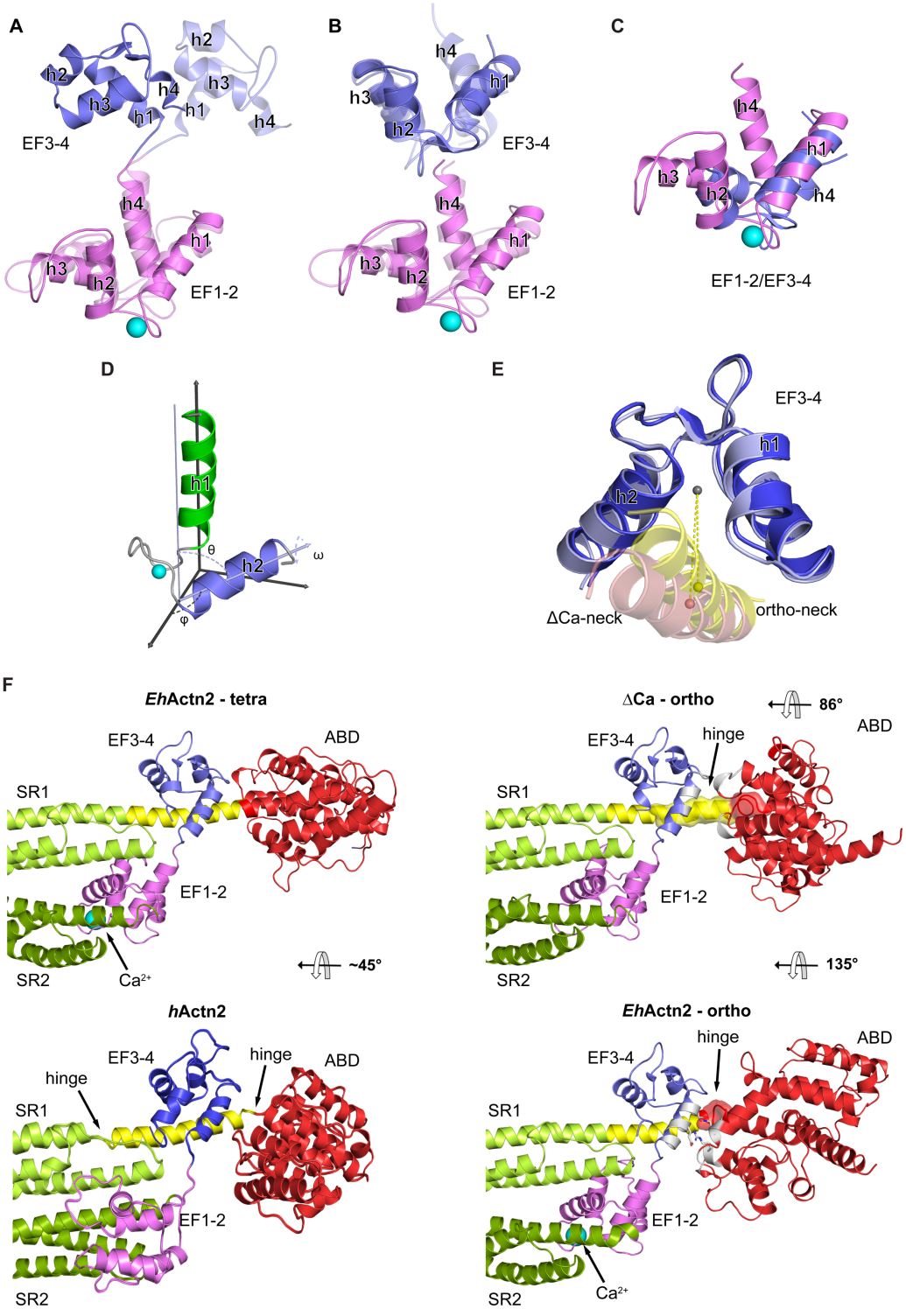

Figure S3. Structural insights into EhActn2 and hActn2 EF hands.

(A) *Eh*Actn2 CaMD adopts different orientations in crystal and in solution, as inferred from the superposition of the CaMD from the *Eh*Actn2 tetragonal structure and a previously reported NMR structure (PDB code 2M7L) fixing EF1-2 (violet; calcium ion in cyan, EF3-4 in blue). CaMDs from the former

and later structure are shown in a solid and transparent ribbon representation, respectively. **(B)** Deviation of helices h1 and h4 in individual CaMD lobes. Superposition of individual EF1-2 and EF3-4 from the same CaMDs as in (A) (same colour code and ribbon representation). **(C)** Superposition of EF1-2 and EF3-4 from the tetragonal *Eh*Actn2 structure (colour code as in (A)). **(D)** Vector geometry mapping representation of a calcium bound EF-hand as defined by (31). **(E)** Superposition of EF3-4 from ΔCa and orthorhombic *Eh*Actn2 structures, together with the corresponding neck regions in pale red and yellow, respectively. The centres of gravity are shown as dots; grey for EF3-4, and pale red and yellow for the neck regions. **(F)** CaMD/neck/ABD conformational changes and interactions in the three determined structures of *Eh*Actn2 plus that of human α-actinin-2 (32), all aligned at SR1-SR2 (colour code as in Figure S1). ABD rotation is indicated in each structure with respect to the orientation found in the tetragonal form. The hinge in the two orthorhombic *Eh*Actn2 structures is highlighted in a transparent surface and indicated with an arrow. Residues involved in interactions between EF3-4 and ABD are coloured in grey.

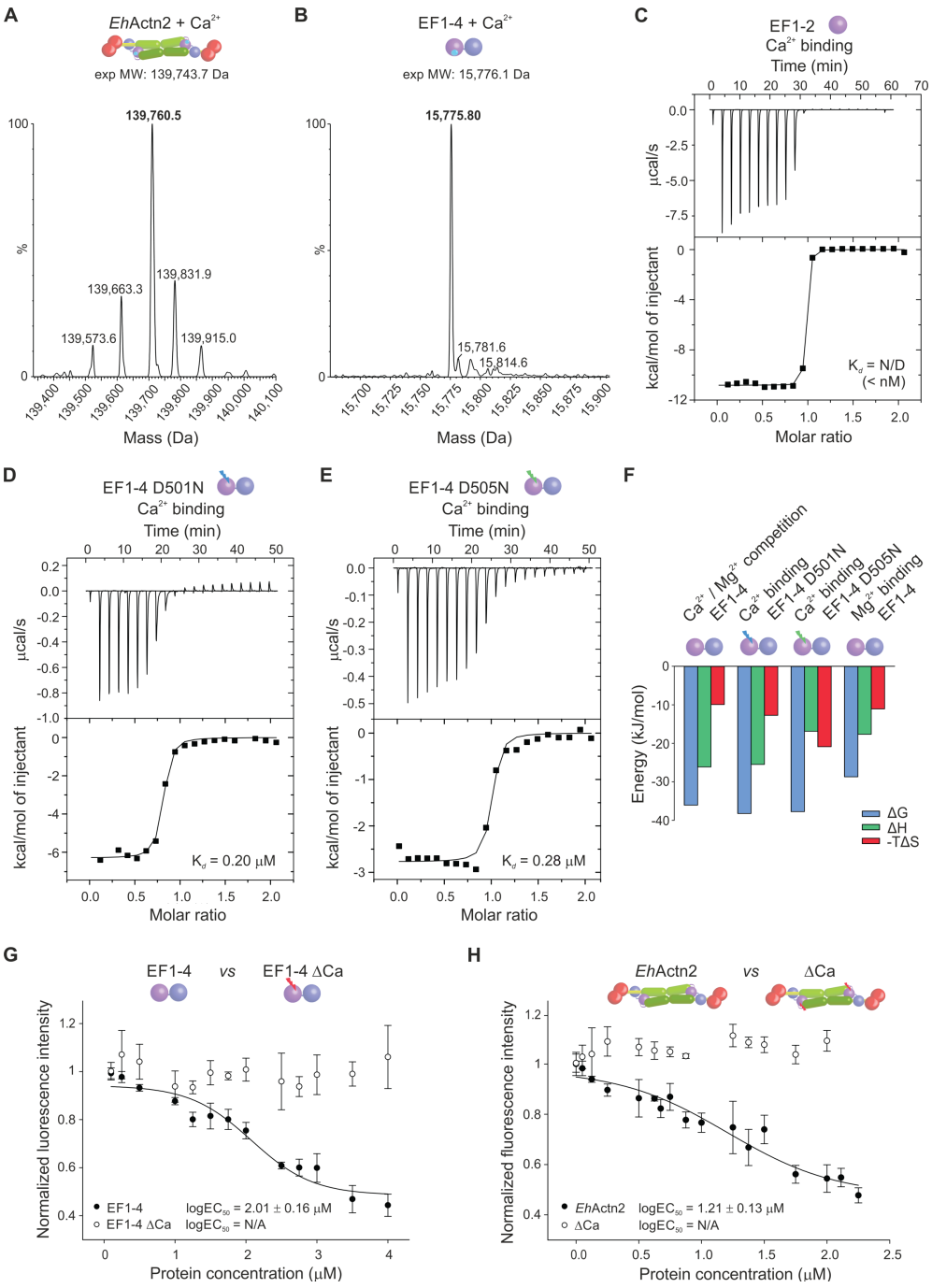

Figure S4. Evidence of Ca2+-binding for EhActn2 EF-hands.

(A, B) Intact mass spectrometry of *Eh*Actn2 and EF1-4 reveals that in both cases one Ca^{2+} ion is bound to the protein. Evidence of Ca^{2+} binding by ITC to EF1-2 **(C)**; to EF1-4 D501N **(D)** and to EF1-4 D505N **(E)**. No K_d value was determined for EF1-2, while for the two mutants the K_d value was in the µM range. **(F)** Thermodynamic parameters of ITC experiments. **(G, H)** Evidence of Ca^{2+} binding as assessed by Ca^{2+}-dye competition assays using Oregon Green 488 BAPTA-5N dye for EF1-4 and *Eh*Actn2 (mean ± standard deviation). Corresponding ΔCa constructs were used as negative controls. For calculation of $logEC_{50}$ values, individual proteins were considered in their respective oligomeric state (i.e. monomer for EF1-4 and dimer for *Eh*Actn2). N/D stands for not determined.

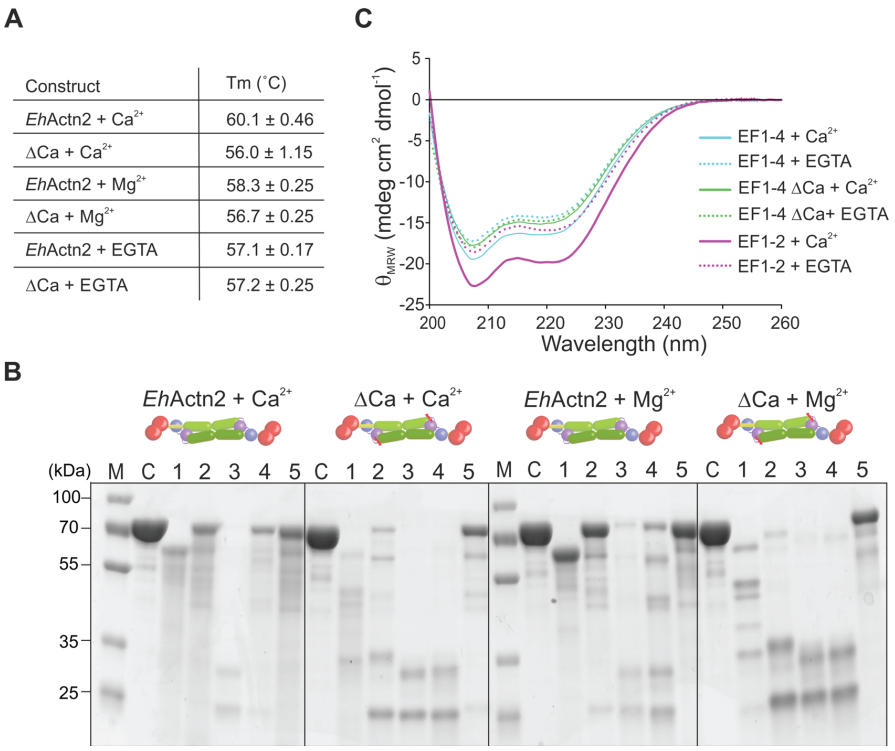

Figure S5. Conformational stability of ion-free and Ca^{2+}- or Mg^{2+}-bound *Eh*Actn2.

(A) Melting temperature (Tm) assessed by differential scanning fluorimetry of *Eh*Actn2 and ΔCa in the absence (EGTA) and presence of Ca^{2+} and Mg^{2+} reveals that both ions increase protein stability. **(B)** Limited proteolysis of *Eh*Actn2 in the absence (ΔCa) and presence of Ca^{2+} and Mg^{2+} support an increased conformational stability for ion-bound proteins. Digested samples were analysed by SDS-PAGE (M and C stand for molecular weight marker and control protein, respectively). Protein incubated with trypsin (lane 1), chymotrypsin (lane 2), proteinase K (lane 3), subtilisin (lane 4) and thermolysin (lane 5). **(C)** Circular dichroism spectra of *Eh*Actn2 EF-hands in the absence (EGTA) and presence of Ca^{2+}.

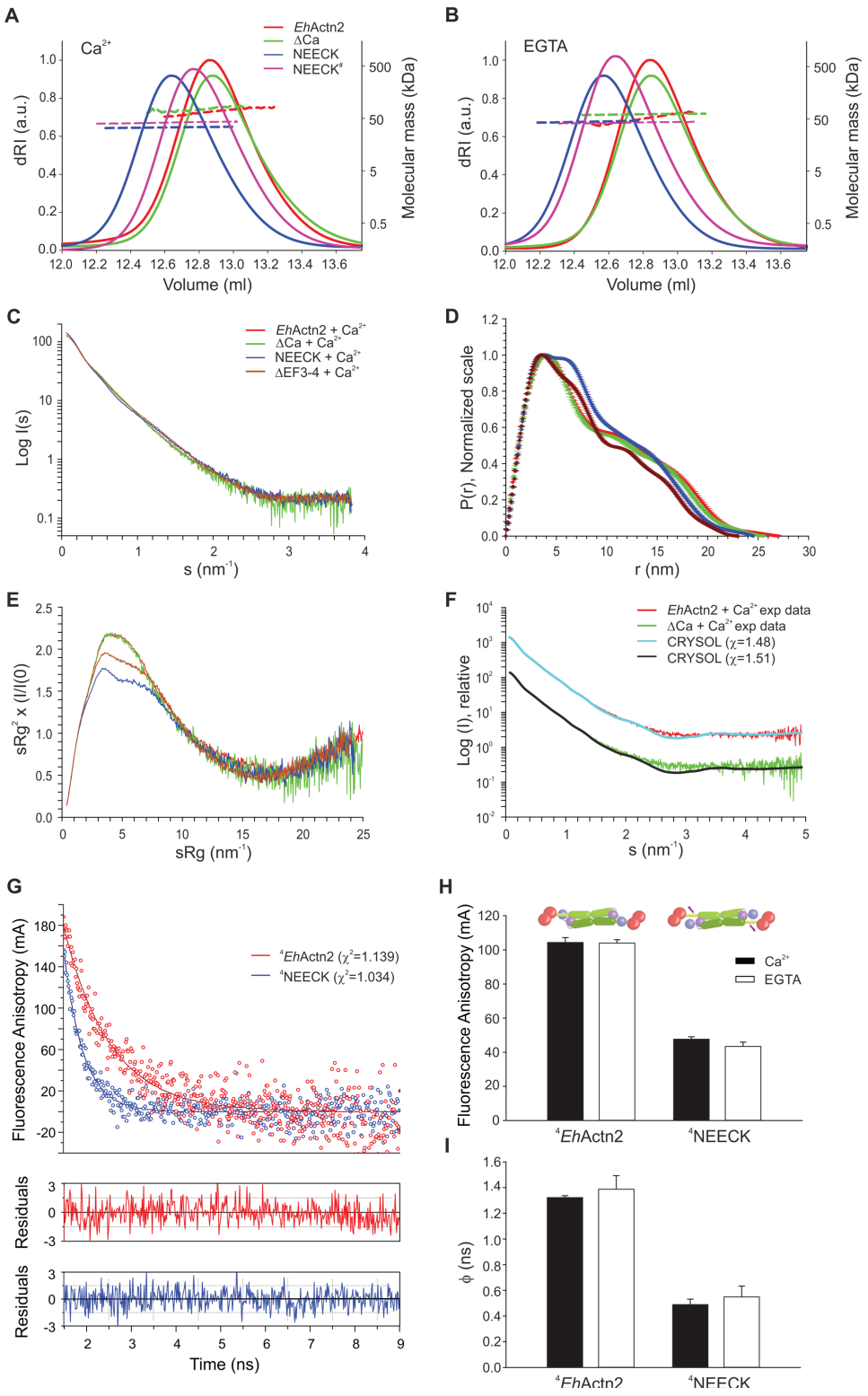

Figure S6. Conformational flexibility of *Eh*Actn2.

(A, B) SEC-MALS of *Eh*Actn2, ΔCa, NEECK and NEECK$^{\#}$ (for details on constructs, see Table S1) performed in Ca^{2+} or EGTA. **(C)** Experimental SAXS data measured for *Eh*Actn2, ΔCa, NEECK and ΔEF3-4 plotted as a function of the momentum transfer. Samples were measured in Ca^{2+} or EGTA resulting in identical profiles

in both buffer conditions (only former samples are shown for clarity). Distance distribution function P(r) **(D)** and Kratky plot **(E)** for the same samples as in (C). **(F)** Fit of Ca^{2+}-bound *Eh*Actn2 and ΔCa structures to experimental SAXS data using program CRYSOL. Time-resolved fluorescence anisotropy **(G)** and rotational lifetime values **(H, I)** of ^{4}*Eh*Actn2 and ^{4}NEECK measured in Ca^{2+} and EGTA (mean ± standard deviation) showing increased conformational stability for the NEECK.

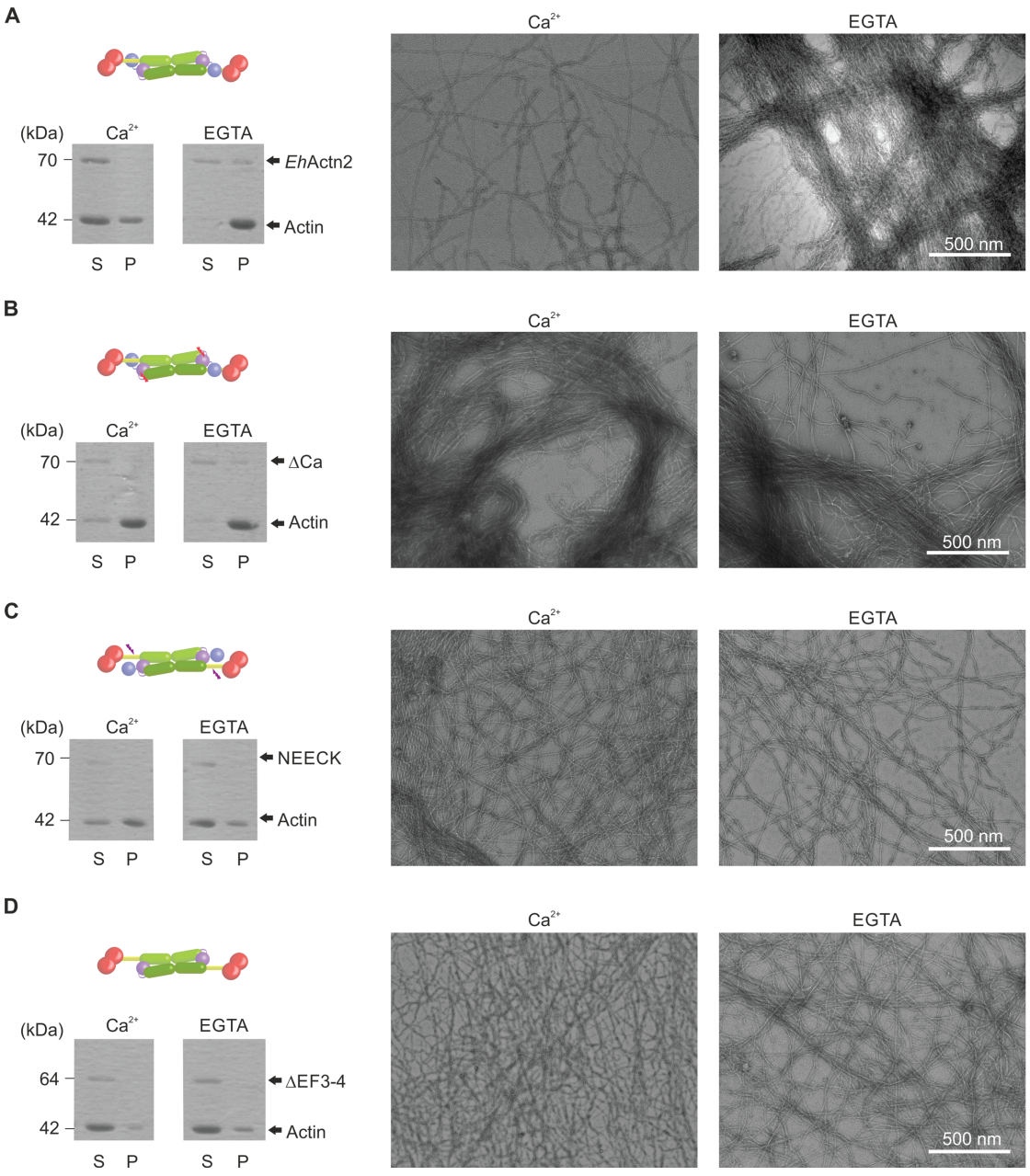

Figure S7. F-actin bundling activity of *Eh*Actn2.

(A-D) F-actin bundling activity of *Eh*Actn2, ΔCa, NEECK and ΔEF3-4 at 0.25 µM measured in Ca^{2+} or EGTA and analysed by SDS-PAGE and EM of negatively stained proteins (S and P stand for supernatant and pellet fractions, respectively; scale bars are indicated). Ca^{2+} inhibits bundling of *Eh*Actn2; ΔCa is insensitive to Ca^{2+}; and NEECK and ΔEF3-4 are incapable of bundling regardless of the presence of Ca^{2+}.

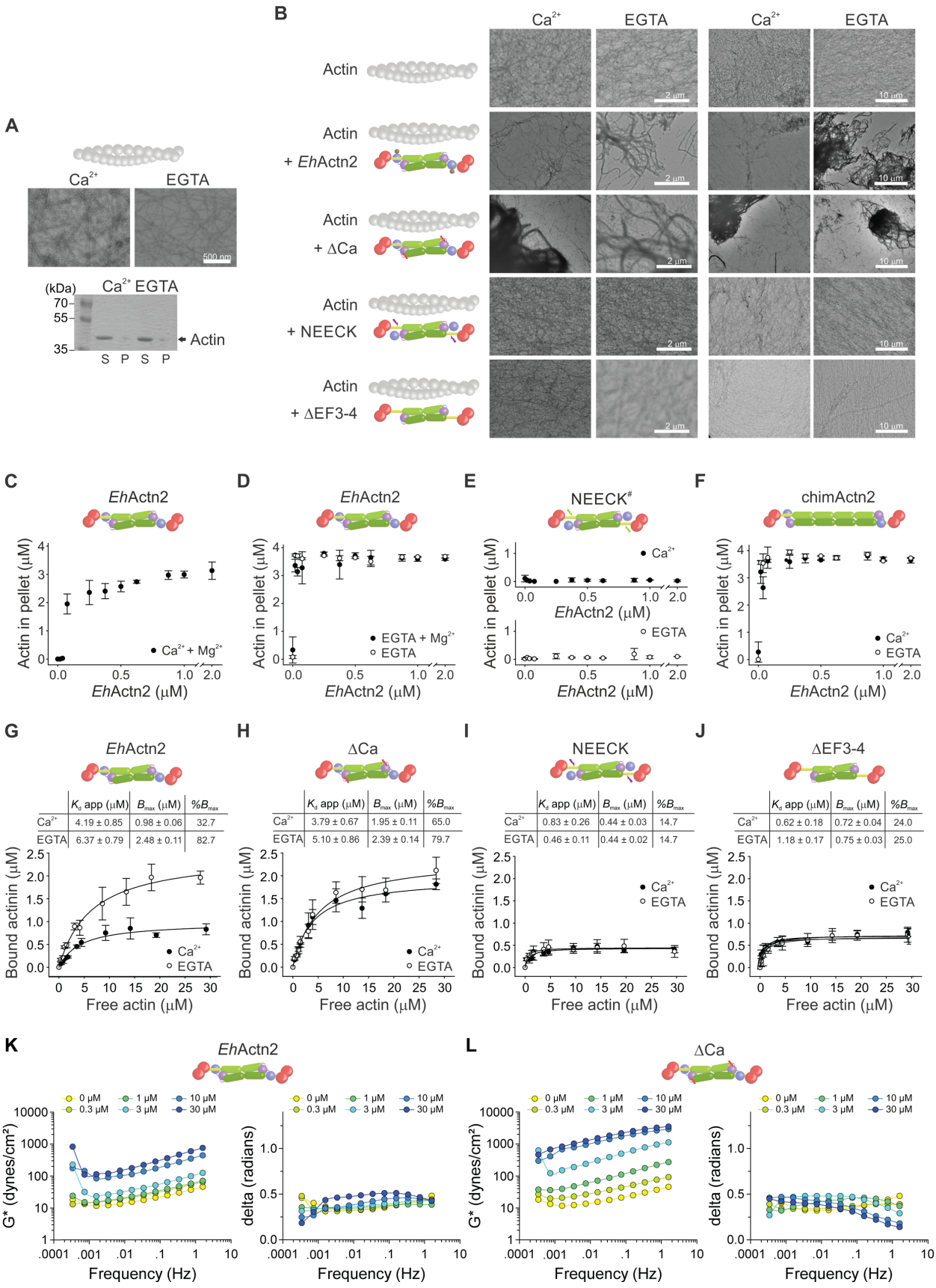
A
Ca2+
EGTA
500 nm
(kDa)
Ca2+ EGTA
70
55
35
Actin
S P S P
B
Ca2+
EGTA
Ca2+
EGTA
Actin
Actin
+ EhActn2
Actin
+ ΔCa
Actin
+ NEECK
Actin
+ ΔEF3-4
2 μm
10 μm
C
EhActn2
Actin in pellet (μM)
Ca2+ + Mg2+
EhActn2 (μM)
D
EhActn2
Actin in pellet (μM)
EGTA + Mg2+
EGTA
EhActn2 (μM)
E
NEECK#
Actin in pellet (μM)
Ca2+
EhActn2 (μM)
EGTA
EhActn2 (μM)
F
chimActn2
Actin in pellet (μM)
Ca2+
EGTA
EhActn2 (μM)
G
EhActn2
Kd app (μM) | Bmax (μM) | %Bmax
Ca2+ 4.19 ± 0.85 | 0.98 ± 0.06 | 32.7
EGTA 6.37 ± 0.79 | 2.48 ± 0.11 | 82.7
Bound actinin (μM)
Ca2+
EGTA
Free actin (μM)
H
ΔCa
Kd app (μM) | Bmax (μM) | %Bmax
Ca2+ 3.79 ± 0.67 | 1.95 ± 0.11 | 65.0
EGTA 5.10 ± 0.86 | 2.39 ± 0.14 | 79.7
Bound actinin (μM)
Ca2+
EGTA
Free actin (μM)
I
NEECK
Kd app (μM) | Bmax (μM) | %Bmax
Ca2+ 0.83 ± 0.26 | 0.44 ± 0.03 | 14.7
EGTA 0.46 ± 0.11 | 0.44 ± 0.02 | 14.7
Bound actinin (μM)
Ca2+
EGTA
Free actin (μM)
J
ΔEF3-4
Kd app (μM) | Bmax (μM) | %Bmax
Ca2+ 0.62 ± 0.18 | 0.72 ± 0.04 | 24.0
EGTA 1.18 ± 0.17 | 0.75 ± 0.03 | 25.0
Bound actinin (μM)
Ca2+
EGTA
Free actin (μM)
K
EhActn2
0 μM 0.3 μM 1 μM 3 μM 10 μM 30 μM
G* (dynes/cm²)
Frequency (Hz)
delta (radians)
Frequency (Hz)
L
ΔCa
0 μM 0.3 μM 1 μM 3 μM 10 μM 30 μM
G* (dynes/cm²)
Frequency (Hz)
delta (radians)
Frequency (Hz)

Figure S8. F-actin bundling and binding activity of *Eh*Actn2.

(A) F-actin bundling control experiment analysed by SDS-PAGE and EM of negatively stained proteins (S and P stand for supernatant and pellet fractions, respectively; scale bar is indicated). **(B)** F-actin bundling activity of *Eh*Actn2 constructs (*Eh*Actn2, ΔCa, NEECK and ΔEF3-4) at 0.25 μM (F-actin at 4 μM) measured in Ca^{2+} or EGTA and visualized by EM of negatively stained proteins at two different magnifications (scale bars are indicated). **(C)** F-actin bundling activity of *Eh*Actn2 at increasing concentrations (0.01875-3 μM) (F-actin at 4 μM) in Ca^{2+} and Mg^{2+} (mean ± standard deviation; same for (C-J)). **(D)** F-actin bundling activity of *Eh*Actn2 as in (C) but in EGTA or EGTA plus Mg^{2+}. **(E)** F-actin bundling activity of NEECK$^{\#}$ as in (C) but in Ca^{2+} or EGTA. **(F)** As in (E), but for chimActn2. **(G-J)** F-actin binding activity of *Eh*Actn2 constructs (as in (B) but at 3 μ M) measured at increasing actin concentrations (0-30 μM) in Ca^{2+} or EGTA. Binding parameters were calculated according to a one-site saturation model, showing increased binding affinity and decreased stoichiometry for NEECK and ΔEF3-4 compared to *Eh*Actn2 and ΔCa. For K_d calculations, a 1:1 stoichiometry was assumed. Rheology data showing the magnitude and phase shift of the complex modulus for-F-actin alone (15 μM) or mixed with increasing concentrations of **(K)** *Eh*Actn2 or **(L)** ΔCa.

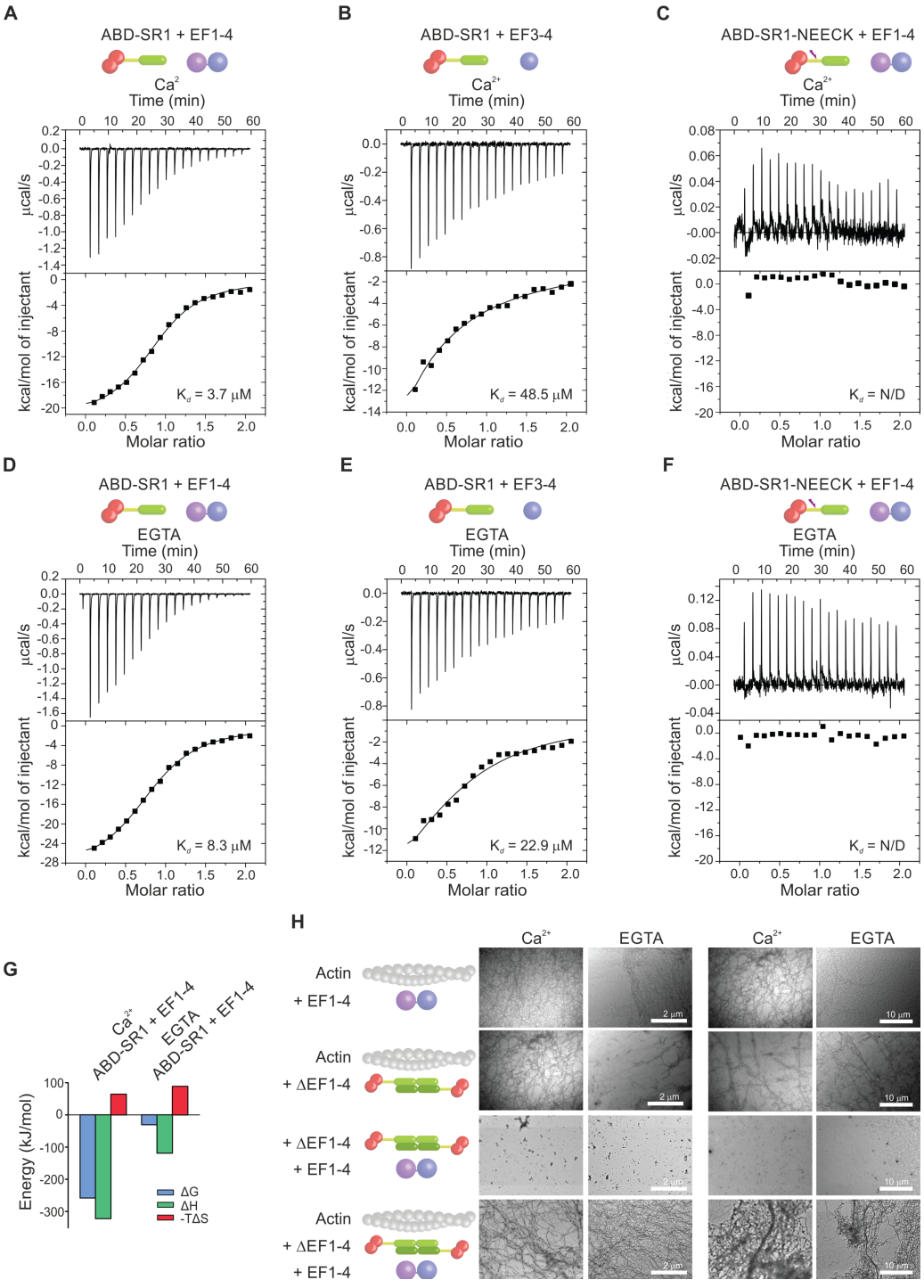

Figure S9. F-actin bundling "rescue" experiments of *Eh*Actn2.

ITC profiles of **(A, D)** EF1-4 binding to ABD-SR1 (for details on constructs, see Table S1) in Ca^{2+} or EGTA; **(B, E)** EF3-4 binding to ABD-SR1 in Ca^{2+} or EGTA; **(C, F)** EF1-4 binding to ABD-SR1-NEECK in Ca^{2+} or EGTA. No K_d value was determined for EF1-4 to ABD-SR1-NEECK, while the K_d value for EF1-4 and EF3-4 to ABD-SR1 was in the µM range. **(G)** Thermodynamic parameters of ITC experiments. **(H)** F-actin bundling "rescue" experiments of ΔEF1-4 plus EF1-4 visualized by EM of negatively stained proteins at two different magnification (scale bars are indicated).

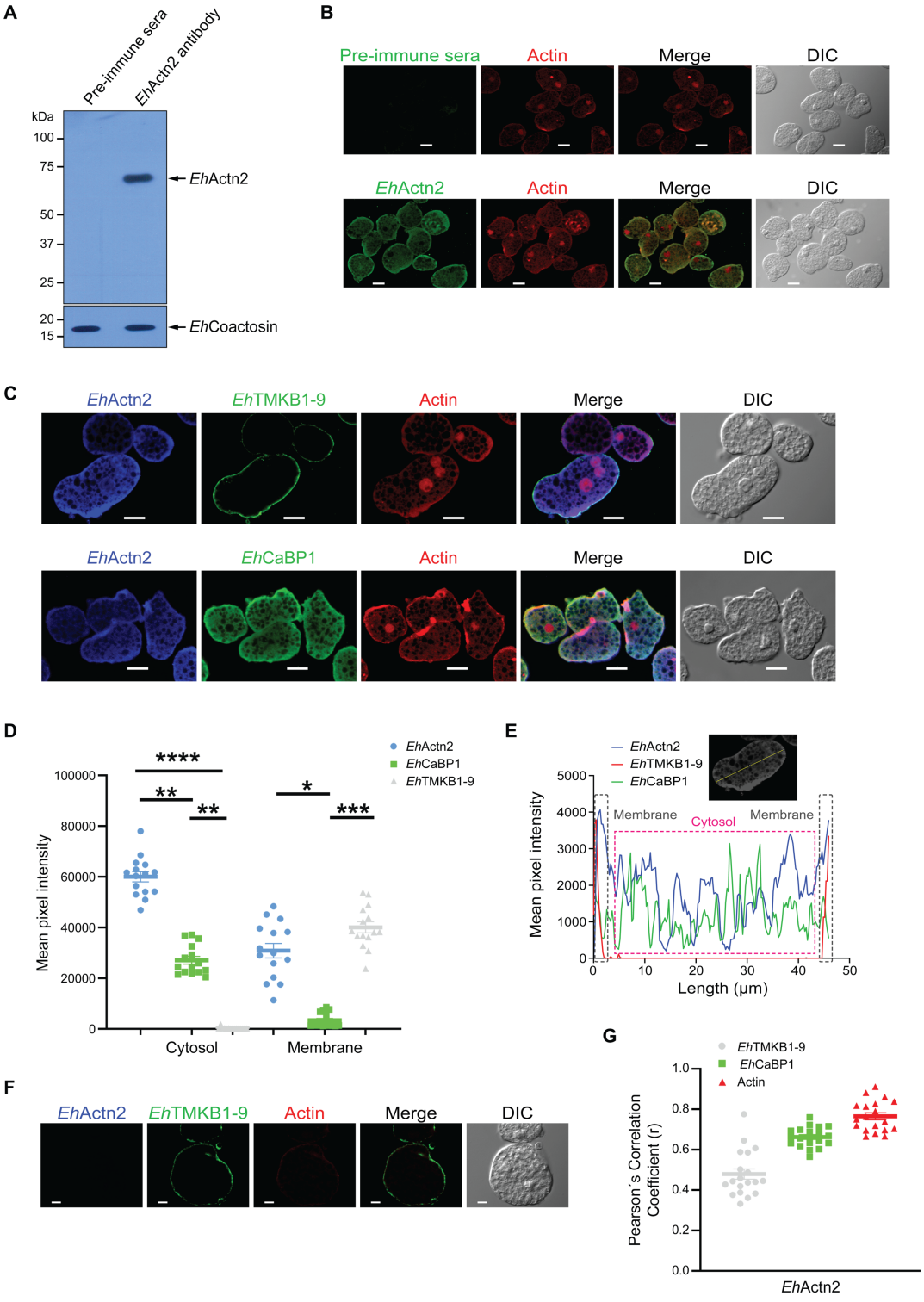

Figure S10. *Eh*Actn2 antibody specificity and cellular localization in *E. histolytica*.

(A) Western blotting of *E. histolytica* lysate using anti-*Eh*Actn2 antibody, which showed high specificity. Expected molecular weight of *Eh*Actn2 monomer is 70 kDa. Pre-immune sera and anti-*Eh*Coactosin were used as controls. **(B)** Immunofluorescence imaging of *Eh*Actn2 and actin in *E. histolytica* trophozoites using

pre-immune sera and anti-*Eh*Actn2 (scale bar, 5 μm). **(C)** Immunofluorescence imaging of *Eh*Actn2, *Eh*CaBP1, *Eh*TMKB1-9 and actin in *E. histolytica* trophozoites[#], revealing *Eh*Actn2 localization to both cell membrane and cytoplasm. **(D)** Quantitative analysis of fluorescence intensity of same proteins as in (C) (mean ± standard error). Mean pixel intensity was taken from multiple sites from membrane and cytoplasma for *Eh*Actn2, cytoplasma for *Eh*CaBP1, and membrane for *Eh*TMKB1-9. Average intensity was calculated from 15 cells. Kruskal-Wallis test followed by Dunn's multiple comparison test was used for statistical comparisons (*p-value≤0.05, **p-value≤0.005, ***p-value≤0.0005). **(E)** Intensity profiles representing the fluorescence intensity of *Eh*Actn2, *Eh*TMKB1-9 and *Eh*CaBP1 in cytoplasm and membrane. Snapshot of ROI (a line across the cell) for single cell quantification is also shown. **(F)** Immunofluorescence imaging of *Eh*Actn2, *Eh*TMKB1-9 and actin in non-permeabilized trophozoites. **(G)** Quantitative analysis of co-localisation of *Eh*Actn2 with *Eh*TMKB1-9, *Eh*CaBP1 and actin carried out using PCC (r) based on 15 stained images as in (C). [#]Actin spots observed in TRITC phalloidin staining suggest the presence of other actin-mediated processes in which α-actinin is not involved. Accordingly, we do not observe co-localization of actin with α-actinin at those spots.

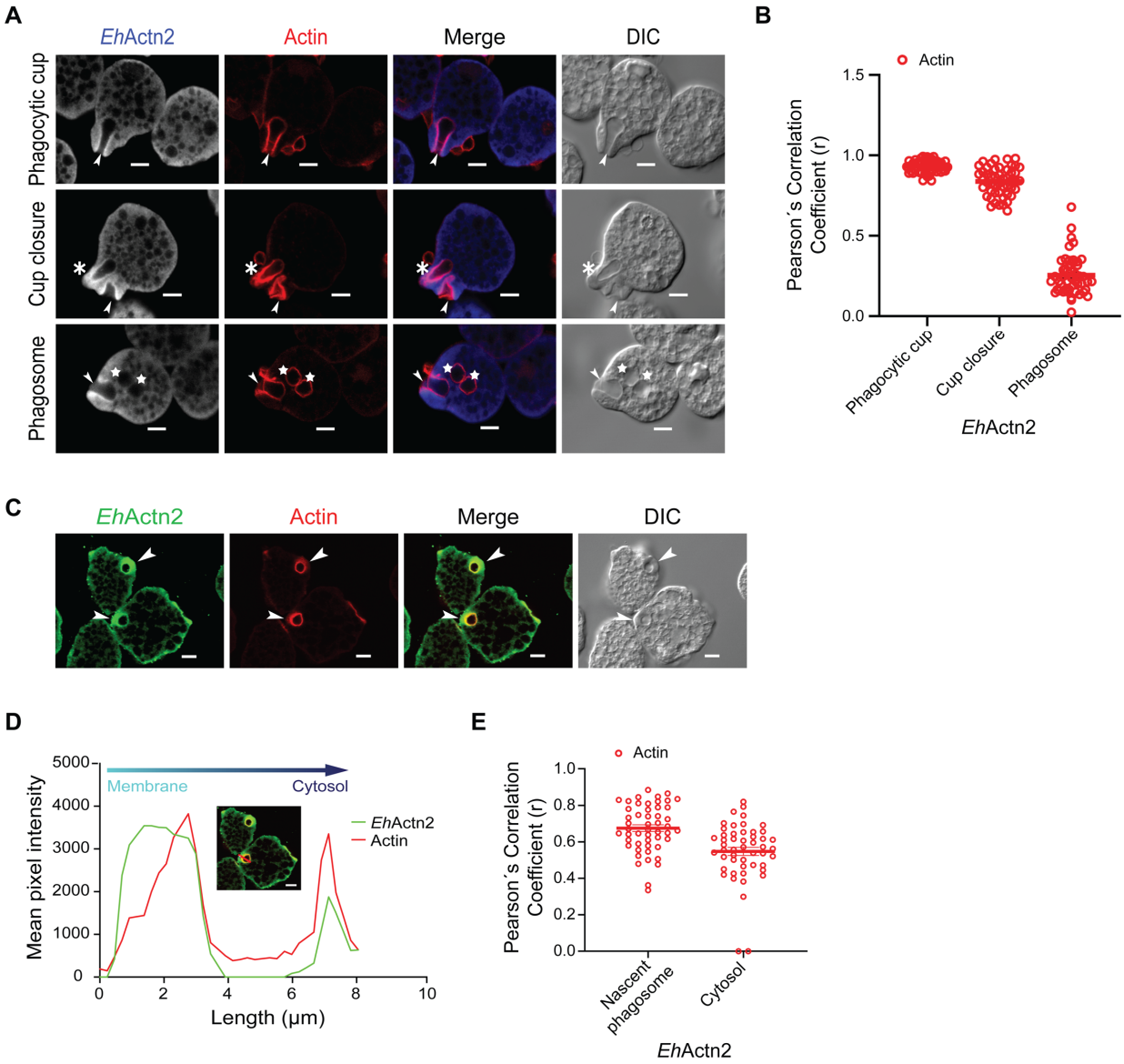

Figure S11. Effect of EhActn2 in erythrophagocytosis.

(A) Immunofluorescence imaging of *Eh*Actn2 in trophozoites incubated with human RBCs, revealing the presence of *Eh*Actn2 at different phagocytic structures, from cups to closure of cups until the process of scission, but not in mature phagosomes. Arrowheads, asterisks and stars indicate phagocytic cups, closed cups (just before scission) and phagosomes, respectively (scale bar, 5 µm). Alexa 405 staining of *Eh*Actn2 is pseudo-coloured to grey. **(B)** Quantitative analysis of co-localisation of *Eh*Actn2 with actin at different stages of erythrophagocytosis carried out using PCC (r) based on 50 events for each stage. **(C)** Immunofluorescence imaging of EhActn2 and actin in trophozoites incubated with human RBCs for 7 min. Nascent phagosomes are marked with an arrowhead. (D) Intensity profiles representing the distribution of pixel intensity of EhActn2 and actin across the nascent phagosome as in (C). (E) Quantitative analysis of co-localisation of EhActn2 with actin in nascent phagosomes as in (C) using PCC (r) based on 50 events (mean ± standard error).

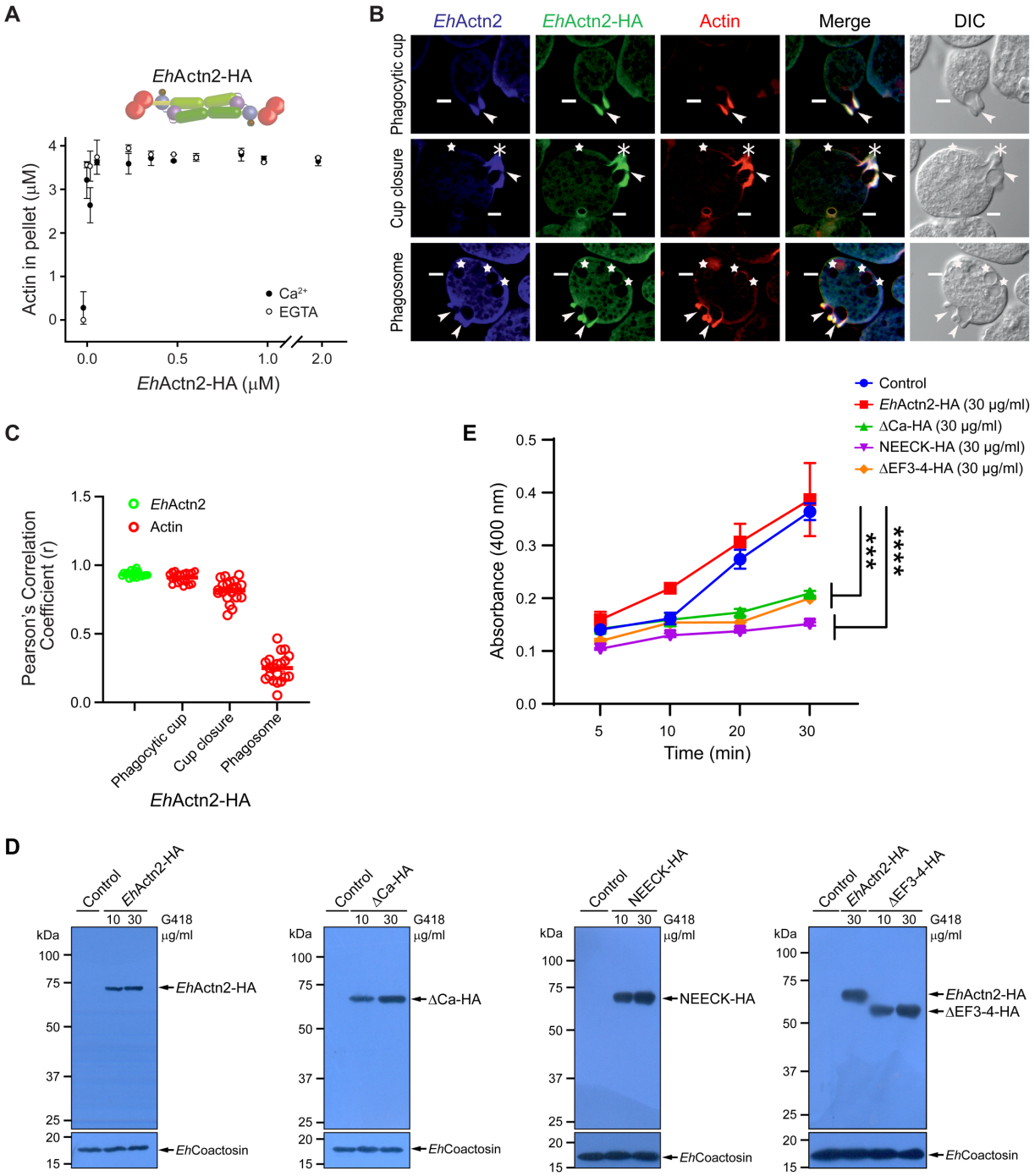

Figure S12. Effect of HA tag and mutations on *Eh*Actn2 cellular localisation and erythrophagocytosis.

(A) F-actin bundling activity of *Eh*Actn2-HA in Ca^{2+} or EGTA as in Fig. S8 (mean ± standard deviation). **(B)** Immunofluorescence imaging of endogenous *Eh*Actn2, *Eh*Actn2-HA and actin in *E. histolytica* trophozoites. Arrowheads, asterisks and stars indicate phagocytic cups, closed cups (just before scission) and phagosomes, respectively (scale bar, 5 μm). **(C)** Quantitative analysis of co-localisation of *Eh*Actn2-HA with endogenous *Eh*Actn2 and actin at different stages of erythrophagocytosis using PCC (r) based on 20 events for each stage (mean ± standard error; same for (D)). **(D)** Western blotting using anti-HA and anti-

*Eh*Coactosin antibodies of trophozoites harbouring empty vector (Control) or overexpressing *Eh*Actn2-HA constructs in 10 µg/ml or 30 µg/ml G418. **(E)** Quantitative analysis of erythrocyte uptake in trophozoites harbouring empty vector (Control) or overexpressing *Eh*Actn2-HA constructs (*Eh*Actn2-HA, ΔCa-HA, NEECK-HA and ΔEF3-4-HA) in 30 µg/ml G418, showing a reduction in uptake of 45%, 60% and 48% in cells overexpressing ΔCa-HA, NEECK-HA and ΔEF3-4-HA, respectively at 30 min. One-way Anova was used for statistical comparisons against empty vector (control) grown using 30 µg/ml G418 (*p-value≤0.05, **p-value≤0.005, **p-value≤0.0005).

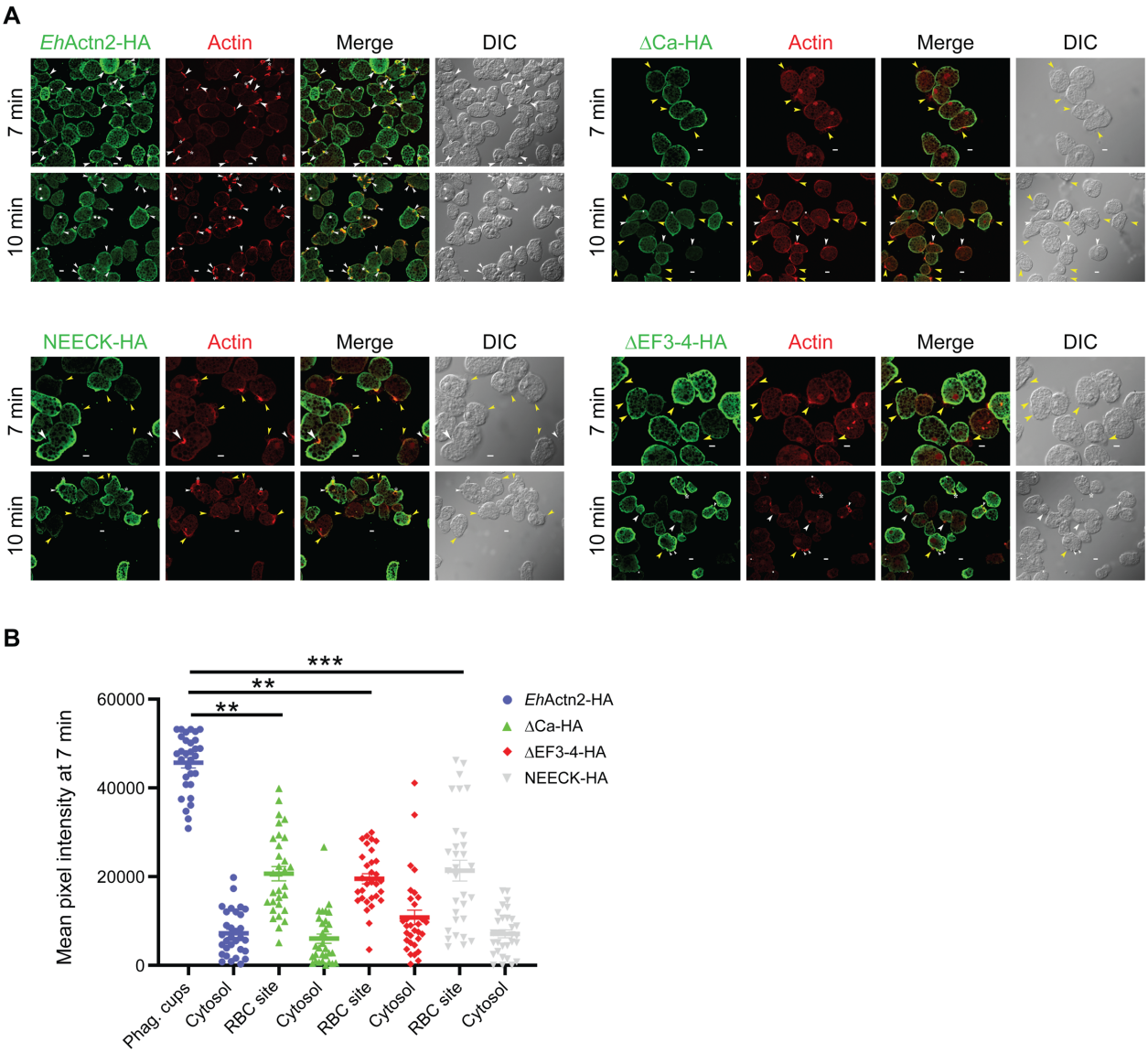

Figure S13. Erythrophagocytosis in cells expressing *Eh*Actn2 variants.

(A) Immunofluorescence imaging of overexpressed *Eh*Actn2 constructs (*Eh*Actn2-HA, ΔCa-HA, NEECK-HA and ΔEF3-4-HA) and actin in *E. histolytica* trophozoites incubated with human RBCs for 7 and 10 min. Arrowheads, asterisks, stars and yellow arrowheads indicate phagocytic cups, closed cups (just before scission), phagosomes and RBCs attached at the site of phagocytosis, respectively (scale bar, 5 µm). **(B)** Quantitative analysis of fluorescent intensity of *Eh*Actn2 constructs (*Eh*Actn2-HA, ΔCa-HA, NEECK-HA and ΔEF3-4-HA) in trophozoites as in (A) (mean ± standard error). Mean pixel intensity was taken from multiple sites from phagocytic cups and cytosol for *Eh*Actn2-HA, and from RBC attachment site and cytosol for the rest of *Eh*Actn2 variants, showing that ΔCa-HA, NEECK-HA and ΔEF3-4-HA are not recruited to phagocytic cups. Average intensity was calculated from 25 cells. Kruskal-Wallis test followed by Dunn's multiple comparison test were used for statistical comparisons (*p-value≤0.05, **p-value≤0.005, ***p-value≤ 0.0005).

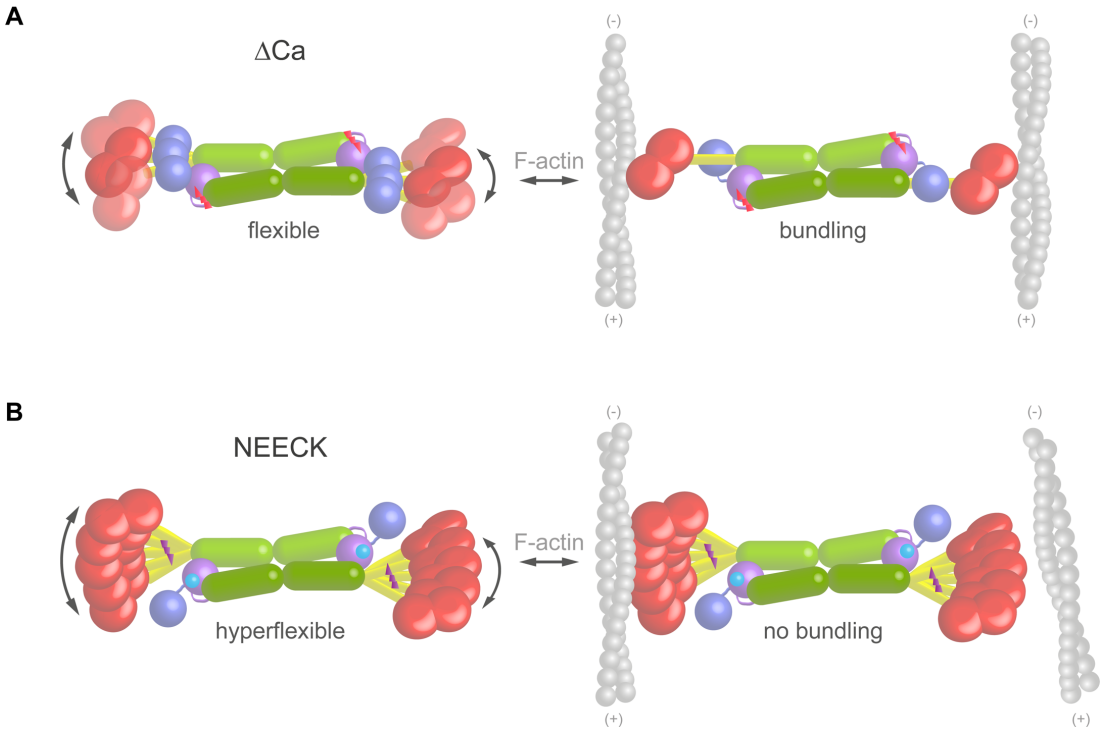

Figure S14. Working model for Ca^{2+} regulation and bundling in *Eh*Actn2 variants.

(A, B) Schematics illustrating the molecular mechanism by which ΔCa and NEECK are constitutively activated and inactivated F-actin bundlers, respectively. *Eh*Actn2 domains are shown as in Figure S1. Ca^{2+} ion is shown as a cyan sphere.

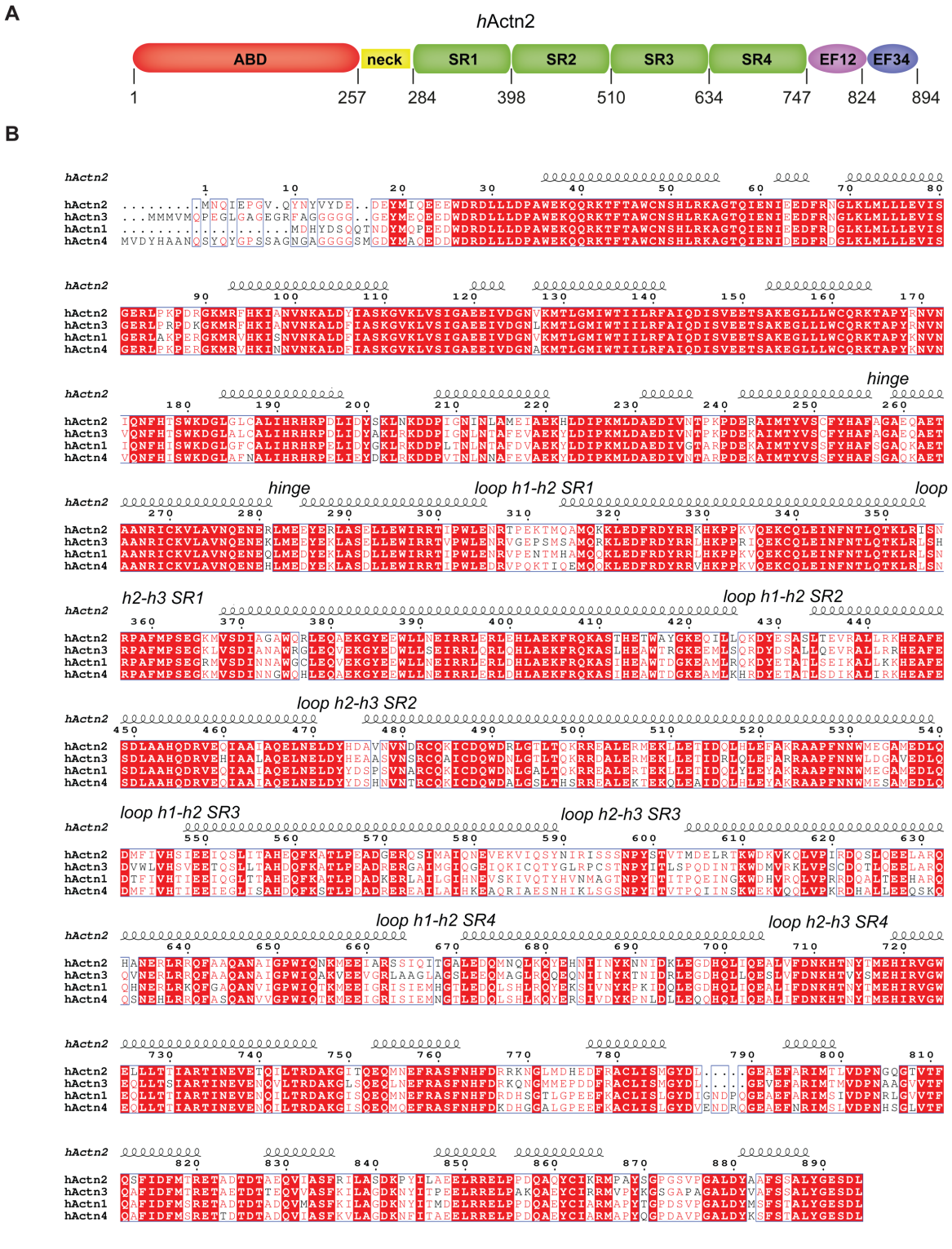
A
hActn2
ABD
neck
SR1
SR2
SR3
SR4
EF12
EF34
1
257
284
398
510
634
747
824
894
B
hinge
loop h1-h2 SR1
loop
h2-h3 SR1
loop h1-h2 SR2
loop h2-h3 SR2
loop h1-h2 SR3
loop h2-h3 SR3
loop h1-h2 SR4
loop h2-h3 SR4
C
EF3-4
SR1
SR2
SR3
SR4
EF3-4
neck
neck
SR2
ABD
ABD
EF1-2
EF1-2

Figure S15. Domain boundaries and sequence alignment of human α-actinins.

(A) Domain boundaries of *h*Actn2 sequence from UP code P35609. **(B)** Sequence alignment of human α-actinins (*h*Actn2; *h*Actn3, UP code Q08043; *h*Actn1, UP code P12814; and *h*Actn4, UP code O43707) performed with MULTIALIN (33) and represented using the ESPript server (34). Secondary structure elements, hinges and SR loops based on *h*Actn2 crystal structure (32) are indicated. **(C)** Structure of *h*Actn2 in a ribbon representation coloured based on residue conservation among human α-actinins (blue corresponding to conservation=0.25, red to conservation=1; figure made with Chimera (35)).

SUPPLEMENTARY REFERENCES

1. W. Rauert, A. N. Eddine, S. H. Kaufmann, M. S. Weiss, R. Janowski, Reductive methylation to improve crystallization of the putative oxidoreductase Rv0765c from Mycobacterium tuberculosis. *Acta crystallographica. Section F, Structural biology and crystallization communications* **63**, 507-511 (2007).
2. J. A. Spudich, S. Watt, The regulation of rabbit skeletal muscle contraction. I. Biochemical studies of the interaction of the tropomyosin-troponin complex with actin and the proteolytic fragments of myosin. *J Biol Chem* **246**, 4866-4871 (1971).
3. D. Franke *et al.*, ATSAS 2.8: a comprehensive data analysis suite for small-angle scattering from macromolecular solutions. *J Appl Crystallogr* **50**, 1212-1225 (2017).
4. W. Kabsch, XDS. *Acta Crystallogr D Biol Crystallogr* **66** (2010).
5. A. Vagin, A. Teplyakov, Molecular replacement with MOLREP. *Acta Crystallogr D Biol Crystallogr* **66**, 22-25 (2010).
6. P. D. Adams *et al.*, PHENIX: a comprehensive Python-based system for macromolecular structure solution. *Acta Crystallogr D Biol Crystallogr* **66**, 213-221 (2010).
7. P. Emsley, B. Lohkamp, W. G. Scott, K. Cowtan, Features and development of Coot. *Acta Crystallogr D Biol Crystallogr* **66**, 486-501 (2010).
8. G. M. Sheldrick, Experimental phasing with SHELXC/D/E: combining chain tracing with density modification. *Acta Crystallogr D Biol Crystallogr* **66**, 479-485 (2010).
9. S. X. Cohen *et al.*, ARP/wARP and molecular replacement: the next generation. *Acta Crystallogr D Biol Crystallogr* **64**, 49-60 (2008).
10. M. D. Winn *et al.*, Overview of the CCP4 suite and current developments. *Acta Crystallogr D Biol Crystallogr* **67**, 235-242 (2011).
11. A. J. McCoy *et al.*, Phaser crystallographic software. *J Appl Crystallogr* **40**, 658-674 (2007).
12. O. Kovalevskiy, R. A. Nicholls, G. N. Murshudov, Automated refinement of macromolecular structures at low resolution using prior information. *Acta Crystallographica Section D: Structural Biology* **72**, 1149-1161 (2016).
13. E. Krissinel, K. Henrick, Inference of macromolecular assemblies from crystalline state. *J Mol Biol* **372**, 774-797 (2007).
14. E. Krissinel, K. Henrick, Secondary-structure matching (SSM), a new tool for fast protein structure alignment in three dimensions. *Acta Crystallogr D Biol Crystallogr* **60**, 2256-2268 (2004).
15. S. Hayward, H. J. Berendsen, Systematic analysis of domain motions in proteins from conformational change: new results on citrate synthase and T4 lysozyme. *Proteins* **30**, 144-154 (1998).
16. N. A. Baker, D. Sept, S. Joseph, M. J. Holst, J. A. McCammon, Electrostatics of nanosystems: application to microtubules and the ribosome. *Proceedings of the National Academy of Sciences* **98**, 10037-10041 (2001).
17. T. J. Dolinsky, J. E. Nielsen, J. A. McCammon, N. A. Baker, PDB2PQR: an automated pipeline for the setup of Poisson–Boltzmann electrostatics calculations. *Nucleic acids research* **32**, W665-W667 (2004).
18. K. L. Yap, J. B. Ames, M. B. Swindells, M. Ikura, "Vector geometry mapping" in Calcium-Binding Protein Protocols: Volume 2: Methods and Techniques. (Springer, 2002), pp. 317-324.
19. O. Carugo, P. Argos, NADP-dependent enzymes. II: Evolution of the mono- and dinucleotide binding domains. *Proteins* **28**, 29-40 (1997).

20. M. Babuta, M. S. Mansuri, S. Bhattacharya, A. Bhattacharya, The Entamoeba histolytica, Arp2/3 Complex Is Recruited to Phagocytic Cups through an Atypical Kinase EhAK1. *PLoS Pathogens* **11**, e1005310 (2015).
21. B. P. Cormack, R. H. Valdivia, S. Falkow, FACS-optimized mutants of the green fluorescent protein (GFP). *Gene* **173**, 33-38 (1996).
22. M. Babuta, S. Kumar, S. Gourinath, S. Bhattacharya, A. Bhattacharya, Calcium-binding protein EhCaBP3 is recruited to the phagocytic complex of Entamoeba histolytica by interacting with Arp2/3 complex subunit 2. *Cell Microbiol* **20**, e12942 (2018).
23. J. M. de Pereda, M. P. Lillo, A. Sonnenberg, Structural basis of the interaction between integrin alpha6beta4 and plectin at the hemidesmosomes. *EMBO J* **28**, 1180-1190 (2009).
24. J. Sevcik, L. Urbanikova, J. Kost'an, L. Janda, G. Wiche, Actin-binding domain of mouse plectin. Crystal structure and binding to vimentin. *Eur J Biochem* **271**, 1873-1884 (2004).
25. N. J. Haywood *et al.*, Hypertrophic cardiomyopathy mutations in the calponin-homology domain of ACTN2 affect actin binding and cardiomyocyte Z-disc incorporation. *The Biochemical journal* **473**, 2485-2493 (2016).
26. E. Borrego-Diaz *et al.*, Crystal structure of the actin-binding domain of alpha-actinin 1: evaluating two competing actin-binding models. *J Struct Biol* **155**, 230-238 (2006).
27. G. Franzot, B. Sjoblom, M. Gautel, K. Djinovic Carugo, The crystal structure of the actin binding domain from alpha-actinin in its closed conformation: structural insight into phospholipid regulation of alpha-actinin. *J Mol Biol* **348**, 151-165 (2005).
28. S. H. Lee, A. Weins, D. B. Hayes, M. R. Pollak, R. Dominguez, Crystal structure of the actin-binding domain of alpha-actinin-4 Lys255Glu mutant implicated in focal segmental glomerulosclerosis. *J Mol Biol* **376**, 317-324 (2008).
29. B. Addario, L. Sandblad, K. Persson, L. Backman, Characterisation of Schizosaccharomyces pombe alpha-actinin. *PeerJ* **4**, e1858 (2016).
30. A. R. Clark, G. M. Sawyer, S. P. Robertson, A. J. Sutherland-Smith, Skeletal dysplasias due to filamin A mutations result from a gain-of-function mechanism distinct from allelic neurological disorders. *Hum Mol Genet* **18**, 4791-4800 (2009).
31. K. L. Yap, J. B. Ames, M. B. Swindells, M. Ikura, Vector geometry mapping. A method to characterize the conformation of helix-loop-helix calcium-binding proteins. *Methods Mol Biol* **173**, 317-324 (2002).
32. A. Ribeiro Ede, Jr. *et al.*, The structure and regulation of human muscle alpha-actinin. *Cell* **159**, 1447-1460 (2014).
33. F. Corpet, Multiple sequence alignment with hierarchical clustering. *Nucleic Acids Res* **16**, 10881-10890 (1988).
34. X. Robert, P. Gouet, Deciphering key features in protein structures with the new ENDscript server. *Nucleic Acids Res* **42**, W320-324 (2014).
35. E. F. Pettersen *et al.*, UCSF Chimera--a visualization system for exploratory research and analysis. *J Comput Chem* **25**, 1605-1612 (2004).